Numerical Analysis of Transpiration Cooling on a Turbulent Flat Plate

by

Nicholas Christopher

A thesis
presented to the University of Waterloo
in fulfillment of the
thesis requirement for the degree of
Master of Applied Science
in
Mechanical Engineering

Waterloo, Ontario, Canada, 2019

This thesis consists of material all of which I authored or co-authored: see Statement of Contributions included in the thesis. This is a true copy of the thesis, including any required final revisions, as accepted by my examiners.

I understand that my thesis may be made electronically available to the public.

Statement of Contributions

Contents in Chapters 3-6 have been incorporated within a book chapter in the Proceedings of the 2019 SFB/TRR40 Summer Program [1] that was co-authored by myself, my supervisor (Dr. Jean-Pierre Hickey), Dr. Markus Kloker, and PhD student Johannes Peter. Additionally, contents in Section 2.2, and Chapters 3-6 have been incorporated within a manuscript submitted for publication [2] that was co-authored by myself, my supervisor (Dr. Jean-Pierre Hickey), Dr. Markus Kloker, and PhD student Johannes Peter. I am the first author and main contributor for both of these works. Dr. Kloker and Mr. Peter assisted with the discussion of the results, and editing of the manuscript and the book chapter. Additionally, Mr. Peter provided the post-processing code to compute the λ_2-criteria in Section 5.5. I did the remainder of the work, which was supervised by Dr. Jean-Pierre Hickey.

Abstract

Transpiration cooling is a promising thermal protection system for gas turbines, atmospheric re-entry heat shields, and rocket engine combustion chambers. Design of transpiration cooling systems must rely on numerical simulation in order to reduce costs. The purpose of this work it to better understand the physical phenomena which effect turbulence and heat transfer in a turbulent boundary layer with transpiration cooling, in order to inform models of the system. Towards this goal, direct numerical simulations (DNS) of transpiration cooling in a turbulent flat-plate boundary layer at a freestream mach number of 0.3 have been performed. The coolant and the hot gas are both air, and isothermal walls and coolant at a temperature ratio of $T_w/T_\infty = 0.5$ have been prescribed. The blowing ratio (which is the mass flux ratio between the coolant and the freestream gas), and the coolant injection boundary conditions have been varied to investigate their effects on the flow. It is found that by increasing the blowing ratio, the peak turbulent kinetic energy moves away from the wall to a region of shear between the low-momentum coolant and high-momentum hot gas. As the blowing ratio is increased, there is also a reduction in heat transfer to the porous wall. This reduction of wall heat transfer is caused by the combined effects of heat advection due to the non-zero wall-normal velocity at the wall, and the reduction of the average boundary-layer temperature due to the accumulation of coolant. A new model for the latter effect is proposed which is physically realistic in the limit cases. The proposed combined model accounts for both heat advection and film accumulation and shows good agreement with the DNS data. An increase in turbulent transport of heat with increasing blowing rate is caused by the production of vortices between the coolant and hot gas. This causes a reduction in the cooling effectiveness, and can be seen near the leading edge of the transpiration region. Log law scaling of the velocity profile with blowing walls is analyzed, and found to only be applicable for modest blowing rates. Reasons for the failure of scaling laws at high blowing rates are proposed based on the x-momentum balance of the Navier-Stokes equations. In order to investigate wall modelling effects, simulations with uniform coolant injection have been compared to simulations with injection via many small slits. It is observed that as the slits get smaller (at fixed total mass flow rate and fixed wall porosity), the results trend towards the uniform injection case. Therefore, it is hypothesized that for small pore sizes, neglecting the effects of the individual pores in the wall boundary condition is physically justifiable.

Acknowledgements

I would like to thank Dr. Jean-Pierre Hickey for his guidance with my master's work. I will remember the things I learned from him for the rest of my life. I would also like to thank the rest of the multi-physics interaction lab, for providing a friendly and positive environment to do research.

I would like to thank Markus Kloker and Johannes Peter for their support during my time in Germany. The discussions we had were invaluable to my understanding of fluid mechanics.

I would also like to thank my family. I am forever grateful for the people you are. To my parents and grandparents, thank you for the opportunities you have provided for me through your kindness and hard work.

Finally, I would like to thank Elizabeth O'Sullivan, for giving me the confidence to take on any challenge in my way. I love you to the moon and back!

Dedication

This thesis is dedicated to my family, for their unconditional love and support.

Table of Contents

List of Figures

List of Tables

Abbreviations

AM Additive Manufacturing 6

BC Boundary Condition ix, x, 17, 18, 41–43, 51, 52

CFD Computational Fluid Dynamics 3, 9, 10, 50

CMC Ceramic Matrix Composite 7

CPU Central Processing Unit 15

DLR German Aerospace Center 7

DNS Direct Numerical Simulation 4, 5, 12–15, 20–23, 25, 28, 34, 36–38, 50, 52, 61

RANS Reynolds-Averaged Navier-Stokes 3, 11, 52, 53

SAT Simultaneous Approximation Term 17

SBP Summation-By-Parts 17

SST Shear Stress Transport 3, 11

TKE Turbulent Kinetic Energy 28, 29, 31, 41, 43, 45, 50

TPMM Two-Phase Mixture Model 10, 53

UMZ Uniform Momentum Zone 29

UTZ Uniform Thermal Zone 29

WENO Weighted Essentially Non-Oscillatory 15, 52

Nomenclature

δ_i	inlet boundary layer thickness
δ_{99}	boundary layer thickness based on 99% of the freestream velocity
δ_{ij}	Kronecker delta
$\dot{m}_\infty$	mass flux entering the boundary layer from the freestream
$\dot{m}_c$	mass flux entering the boundary layer from the porous wall
ϵ	porosity
η	cooling effectiveness
κ	log-law multiplication factor
λ	thermal conductivity
λ_2	vortex identification criterion
$\langle T \rangle$	average temperature of the boundary layer
$\mathbf{V}$	time averaged wall-normal Darcy velocity
μ	dynamic viscosity
Ω_{ij}	vorticity tensor
ρ	density
σ	standard deviation

σ_{ij} viscous stress tensor

τ total stress (viscous plus Reynolds)

θ momentum thickness

φ non-dimensional advection/convection parameter $C_p\overline{\rho}_w V_w/h$

B log-law addition factor

B_q non-dimensional wall heat transfer rate $\overline{q}_w/(\overline{\rho}_w C_p u_\tau \overline{T}_w)$

C_p constant pressure heat capacity

e total energy

F blowing ratio $\overline{\rho}_c \mathbf{V}_c/\overline{\rho}_\infty U_\infty$

g gravity

H Heaviside function

h convective heat transfer coefficient

K permeability

k turbulent kinetic energy

L domain size

l_ν viscous length scale

M mach number

N number of samples

Nx, Ny, Nz number of grid points in x, y, and z

P probability

p pressure

q_j heat flux vector

q_w wall heat flux

r	ratio of temperature drop across laminar sublayer to over-all temperature drop
R_{ij}	Reynolds stress
Re_{δ_2}	$\overline{\rho}_\infty U_\infty \theta / \overline{\mu}_w$ momentum thickness Reynolds number using wall viscosity
Re_τ	$\overline{\rho}_w u_\tau \delta_{99} / \overline{\mu}_w$ tau Reynolds number
Re^*_τ	$\sqrt{\overline{\rho}_\infty \overline{\tau}_w} \delta_{99} / \overline{\mu}_\infty$ tau star Reynolds number
Re_θ	$\overline{\rho}_\infty U_\infty \theta / \overline{\mu}_\infty$ momentum thickness Reynolds number
Re_x	Reynolds number from leading edge of plate
s	slot width
S_{ij}	rate-of-strain tensor
SE	uncertainty / standard error
T	temperature
t	time
U	time averaged streamwise velocity
u	streamwise velocity
$u'_{i,rms}$	turbulent intensities $\sqrt{\overline{u'_i u'_i}}$
u_τ	$\sqrt{\overline{\tau}_w / \overline{\rho}_w}$ friction velocity
V	time averaged wall-normal velocity
v	wall-normal velocity
w	spanwise velocity
x	streamwise direction
x'	streamwise distance from the point at which the boundary layer starts
y	wall-normal direction

z spanwise direction

$\overline{()}$ time (or time and spanwise) averaged properties

Subscripts

∞ free stream quantities

a leading edge of transpiration region

ad adiabatic

$advect$ advection effectiveness

b trailing edge of transpiration region

$bulk$ bulk quantites

c coolant quantities at the wall

$film$ film accumulation effectiveness

$flatplate$ evaluated in simulation without coolant injection

I incompressible

i, j, k einstein notation

ref constant reference quantities

res coolant reservoir quantities

tot combined effectiveness

$transpiration$ evaluated in simulation with coolant injection

w wall quantities

$w + 1$ first grid point above wall

Superscripts

$'$ fluctuating component

$+$ inner scaling

Chapter 1

Introduction

Transpiration cooling is a thermal protection system for walls which are exposed to extreme temperatures and convective heat flux. A transpirationally cooled liquid rocket engine is shown in Fig. 1.1. Instead of using a fully solid material, the wall is made porous. Coolant is injected though the porous wall and subsequently enters the hot gas flow above the wall. There are effectively two mechanisms in this system that help to reduce the wall temperature. As the coolant flows through the pores, it absorbs heat from the wall via convection. Additionally, when the coolant exits the porous wall and enters the hot gas flow, it acts to insulate the wall from the hot gas, reducing the heat flux which enters the wall. Transpiration cooling is a very effective cooling method due to the combined effect of these mechanisms.

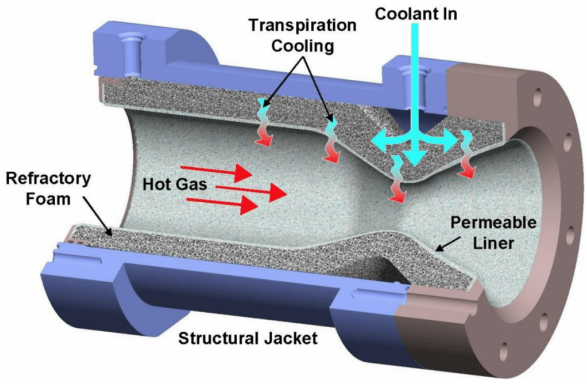

Figure 1.1: Rocket combustion chamber transpiration system. Reprinted from [3].

There are several applications that can benefit from transpirationally cooled walls. Gas turbines often inject coolant through rows of discrete holes on the turbine blades (a method called film cooling) to reduce the blade temperatures [5]. By doing this, the turbine inlet temperature can be increased, resulting in higher system efficiencies. A film cooled gas turbine blade is shown in Fig. 1.2. Since transpiration cooling is often superior to film cooling in terms of cooling effectiveness [6, 7], it is a promising technology in this field. In the space industry, atmospheric re-entry vehicles experience extreme aerothermal heating. Transpiration cooling can be used to build reusable heat shields which require limited maintenance, have rapid turn around times between flights, and use relatively inexpensive wall materials. This is a great benefit in contrast to the previously used technology on the space shuttle. The space shuttle used heat resistant tiles that were fragile, expensive, and required extensive refurbishment between flights (around two man-years for every flight) [8]. There are currently several major organizations considering transpiration cooling for re-entry [9, 10]. Another application in the space industry is the cooling of rocket engine walls. While the current technology (regenerative cooling) works very well [11], there are some applications in which supplemental cooling may be required. Examples of this are small thrusters used for in space missions, and high pressure combustion [12]. Recent work has been done to implement transpiration cooling in rocket engines [13, 14].

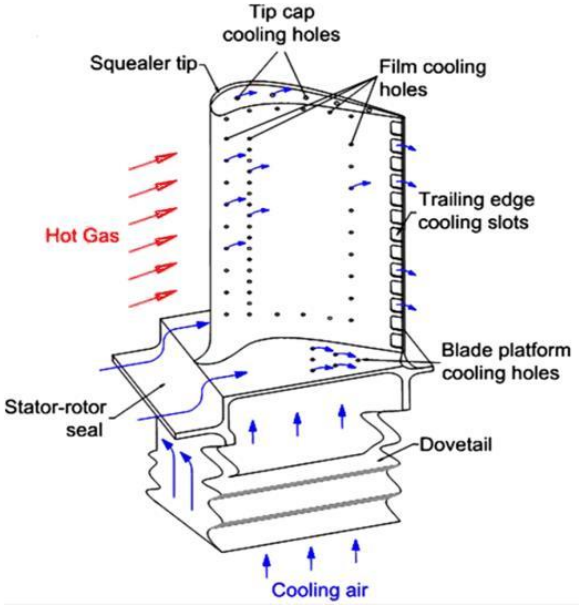

Figure 1.2: Film cooled gas turbine blade. Reprinted from [4].

Aside from heat transfer, there are other physical effects that are caused by transpiration cooling that may be desirable. Notably, there is a reduction of skin friction caused by transpiration cooling [15]. For this reason, injecting fluid into a boundary layer via transpiration has been considered for active drag control [16]. Additionally, the delayed laminar-to-turbulent transition resulting from transpiration cooling may be used to reduce the overall skin friction in aerospace applications [17].

Numerical modelling of fluid and heat transfer can be used as a powerful tool in the design phase of transpiration cooling systems. Since heat fluxes and velocities are often very high, it is difficult and expensive to experimentally test these systems. By using analytical models in the preliminary design phase, and computational fluid dynamics (CFD) in the design optimization phase, the number of parts that need to be manufactured and tested is greatly reduced. This can result in significant savings of time and money, and allow the exploration of new design spaces that may be too challenging to study via experimental tests alone.

In order to model a transpiration cooling system for design optimization, both the porous media and hot gas flows need to be modelled. In the porous medium, the flow of fluid will affect the transfer of heat, and vice versa. The porosity, thermal conductivity, and geometry of the solid material can all affect the system performance. In the hot gas flow, the injected coolant can affect the transfer of heat to the wall, the turbulence, and the drag. Since this is a coupled system, each domain is dependant on the other. Therefore, models of the hot gas and porous media must be coupled together.

For the interaction of the coolant with the hot gas flow, in practical applications the Reynolds-Averaged Navier-Stokes (RANS) equations are used. For the turbulence modelling, the shear-stress transport (SST) model is commonly used, in which a modification at the injection boundary is made in order to account for effects of the injected coolant [18]. However, this correction is based empirically on a very limited set of data, and its validity in cases which are outside of this data set is unclear. More research must be done to investigate the effects of the coolant injection on modifications to the turbulence.

In order to model a transpiration cooling system for design optimization, the porous media and hot gas domain simulations must be coupled. Recently, research has been done towards this goal. For gas-in-gas transpiration cooling, Dahmen et al. [19] have coupled the two domains and compared their results to experiments. For the boundary between the two domains, it is assumed that the coolant is injected uniformly into the hot gas domain (*i.e.* the effects of injecting coolant from individual pores is not modelled). Further research is required in order to validate the assumptions made in the coupling (such as the uniform injection boundary). For the case of initially liquid coolant, no such coupling has been

achieved. Development of a coupled system with coolant changing phase from liquid to vapor is important, since initially liquid coolant is desirable in many applications.

Advances in computational power have enabled researchers to simulate transpiration cooling using direct numerical simulation (DNS). In this approach, the Navier-Stokes equations are solved without any modelling (*i.e.* no turbulence modelling is done). This allows researchers to gain unique insights into the fundamental physics that occurs in transpiration cooling flows. Researchers have preformed incompressible DNS of Couette/Poiseuille flows with one suction and one blowing wall in order to achieve a flow domain independent of streamwise location [20, 21]. Compressible DNS of transpiration coolant injected into a laminar flat plate boundary layer have also been performed [22, 23]. These simulations have been used to gain insights into the physical effects such as drag reduction and turbulence modification, the validity of modelling assumptions, and to propose new models.

In this work, compressible DNS simulations of transpiration coolant injected into a hot gas turbulent flat plate boundary layer have been performed. This type of DNS simulation of transpiration cooling (to the author's knowledge) has never been done before. This case is important since the accumulation of coolant in the boundary layer may affect the amount of heat flux to the wall and the near-wall turbulence. This accumulation affect can only be captured in spatially developing turbulent flows. The amount of coolant injected, as well as the injection boundary conditions have been varied to investigate their effects on the flow. The results of these simulations can be used to inform and validate modelling strategies for transpiration cooling. The main objective of this work is as follows:

- Understand the physical phenomena which affect turbulence and heat transfer in a turbulent flat plate boundary layer with transpiration cooling

In line with this main objective, the secondary objectives are to investigate: (1) the impact of the coolant injection boundary conditions (2) the effect of turbulent structures on the heat transfer (3) low-order modelling of cooling effectiveness (4) log-law velocity modelling.

This thesis is structured in the following format. A literature review of work done in the field of transpiration cooling is provided in Chapter 2. Chapter 3 describes the numerical simulations performed, and Chapter 4 provides validation for the simulations. The results and analysis of the simulations are presented in Chapter 5. The conclusions are presented in Chapter 6, and finally the recommendations for future work are presented in Chapter 7.

Chapter 2

Literature Review

This chapter is broken into four sections. First, the history of transpiration cooling and its applications are discussed in Sec. 2.1. Ultimately, the objective of this thesis is to use DNS to gain insights into the physical phenomena of transpiration cooling. From an applied science perspective, this is done in order to aid in the development of low-order analytical models for the preliminary design phase, and higher order numerical models for the design optimization phase of transpiration cooling systems. For this reason, research in analytical modelling and numerical modelling of transpiration cooling are discussed in Sec. 2.2 and Sec. 2.3 respectively. Section 2.4 provides a literature review of fully resolved DNS, in order to put context to the novelty of the results in this thesis.

2.1 A Brief History of Transpiration Cooling

From the late 1940's and onwards, transpiration cooling has been considered for cooling of aircraft and spacecraft components. Eckert and Livingood [6] compared the effectiveness of convection, film, and transpiration cooling in the 1950's. They did this by using the state of the art analytical modelling tools at the time for the three methods. The results were compared for air-in-air cooling, and showed that transpiration cooling was the most effective method for both laminar and turbulent flows. It was noted that with the addition of high radiation heat transfer, the advantage of using transpiration cooling is reduced. This can be explained by the fact that transpiration cooling reduces the convective heat transfer via heat advection away from the wall, but does nothing to protect against heat transfer to the wall via radiation.

Despite the fact that transpiration cooling is known to be the most effective cooling method in many cases, it has not been used much in practice. This is largely due to the difficulties that arise with manufacturing porous materials. It has been very difficult to manufacture complex shaped porous materials with the desired porosity and permeability. Additionally, porosity is generally detrimental to yield strength and most notably to fatigue strength. This is due to local stress concentrations that occur at the pores, which can result in early crack formation and result in low fatigue strength [24, 25].

Because of the additional complexities of transpiration cooling, film cooling has become a practical alternative. For example, in the manufacturing of turbine blades, the traditional method would be to use investment casting. It is relatively easy to modify this design, and machine discrete holes for film cooling. In contrast, manufacturing a porous wall for transpiration cooling requires alternative manufacturing methods. Figure 1.2 shows a film cooled gas turbine blade. There have been many works since the 1950's aimed at optimizing and informing film cooling design. An excellent summary of analytical modelling theories, and experimental works towards predicting cooling effectiveness prior to the 1970's can be found in Goldstein [26]. Many of the analytical models are based in physics, but have an empirical component to them. This is because the physics is very complex, and factors such as the slot geometry can have a significant effect. For works in film cooling post-1970, the interested reader is referred to the summary by Bogard and Thole [5].

Recently, there has been a surge in transpiration cooling research. This can be seen clearly in Fig 2.1. This increase in interest is driven primarily by two factors. The first is the development of manufacturing methods which enable production of complex-shaped porous materials [7, 27, 28]. The second is the increase in computational power and advances in computational fluid dynamics, which facilitate modelling of the complex system and predictive design optimization.

Recent advances in additive manufacturing (AM) enable the production of porous materials, removing many of the practical issues with transpiration cooling. Research in AM of porous metallic and ceramic materials has been driven largely by the biomedical industry, because of the advantages in bone implants [30]. Due to the methods of manufacturing, it is possible to locally modify the porosity and therefore permeability [27]. This can allow for the optimization of coolant flow through the material, supplying more coolant in the high heat flux regions, and less in the low heat flux regions.

Min et al. [7] have experimentally tested transpiration and film cooling structures produced via additive manufacturing. The material used was Inconel 718, and the manufacturing method was powder bed selective laser metal sintering. Five different pore geometries were produced and compared, as well as one film cooling geometry. They found that the

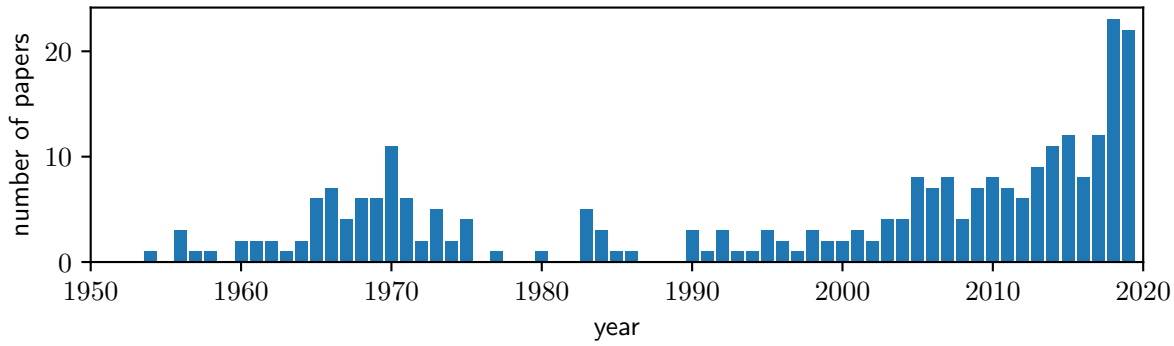

Figure 2.1: Number of publications per year with titles containing "transpiration cooling". Data from [29].

transpirationally-cooled plates generally had a higher cooling effectiveness for the same amount of injected coolant as compared to the film cooled plates. This further confirms the theoretical prediction of transpiration cooling's superiority suggested in the 1950's [6]. The study showed that this method of manufacturing is feasible for applications such as the cooling of gas turbine blades.

For production of ceramic porous materials for transpiration cooling, work has been done recently at the German Aerospace Center (DLR) [28]. They produce porous Ceramic Matrix Composite (CMC) plates, and stack them on top of each other in order to build the combustion chamber of a rocket engine; the testing of the material has been successfully performed in rocket combustion chambers [13]. Aside from combustion chambers, another potential application for this CMC material is the cooling of atmospheric re-entry vehicles [31]. The works mentioned above show that it is feasible to implement transpiration cooling with ceramics in space transportation systems.

2.2 Analytical Modelling

Analytical models can be valuable tools for estimating the wall temperatures in a transpiration cooling system. While analytical models are generally only accurate for simple geometries and well defined cases, they can be used in the preliminary design phase for estimation of the wall temperatures and coolant requirements in order to asses the feasibility of implementing transpiration cooling. Inside the porous domain, in many cases

it can be assumed that the fluid and solid are locally at the same temperature due to the high convective heat transfer between them. Wang and Wang [32] have suggested a criteria for validating this assumption. With this assumption, and assuming a single phase (i.e. gaseous) coolant is used, a 1D energy balance can be used to predict the equilibrium outer/peak wall temperature ($\overline{T}_w$) [6]:

$$\overline{T}_w = \frac{h(1-\overline{\eta})\overline{T}_\infty + \overline{\rho}_w V_w C_p \overline{T}_{res}}{h(1-\overline{\eta}) + \overline{\rho}_w V_w C_p} \tag{2.1}$$

where subscript w denotes fluid properties at the interface between the porous wall and hot gas flow, and ∞ and res denote the hot gas in the free stream and the coolant reservoir temperatures respectively. h denotes the convective heat transfer coefficient between the hot gas and the wall in the case of no transpiration cooling, and $1-\overline{\eta}$ is the average reduction in heat flux due to the injection of coolant. Note that in the case of compressible flow, the hot gas recovery temperature would need to be incorporated.

In Eq. 2.1, the only parameter which is unique to transpiration cooling is the average cooling effectiveness $\overline{\eta}$. There is advection of heat away from the wall due to the non-zero value of V_w. In an attempt to account for this effect, several models for $\overline{\eta}$ were proposed over 50 years ago. The derivations are primarily based on a simplification of the energy equation.

One model for $\overline{\eta}$ developed by Mickley et al. [33] uses a "film theory", in which it is assumed that the heat transfer occurs in a laminar film with a thickness that is chosen to match the actual heat transfer occurring in the turbulent boundary layer. It is clear that this is a fairly crude assumption. Kays and Crawford [34] have also arrived at a similar relationship using a different derivation. Two other models have been derived by Rannie [35] and Friedman [36], by dividing the boundary layer into two regions. The first region is the near-wall flow, in which the turbulent transport of heat is negligible (*i.e.* the viscous sublayer, or the "laminar" layer). The second region is where the turbulence dominates the heat transfer (*i.e.* the log layer). It is assumed that in the turbulent region, the blowing does not significantly affect the heat transfer. However, in the "laminar" layer the heat advection plays a significant role. The equation proposed by Friedman [36] is:

$$\overline{\eta}_{advect} = 1 - \frac{r\varphi}{e^{r\varphi} - 1} \tag{2.2}$$

where φ is:

$$\varphi = \frac{C_p \overline{\rho}_w V_w}{h} \tag{2.3}$$

and r is the ratio of the temperature drop across the laminar sub-layer and the temperature drop across the entire boundary layer. According to [37, 6], the temperature profile can be related to the velocity profile to obtain:

$$r = \frac{2.11}{Re_x^{0.1}} \tag{2.4}$$

It should be noted that the equation for r depends on the Prandtl number, and assumes a turbulent Prandtl number near one. Compared to the equation derived by Mickley et al. [33], Eq. 2.2 has been observed to match the range of experimental data more accurately as noted by Eckert and Livingood [6]. Recent experiments by Langener et al. [38] have suggested that the model by Kays [34] better matches their data for foreign gas transpiration cooling. However, they modify the models to account for the difference in heat capacity, but the modification used appears to be chosen empirically. For the propose of this research, Eq. 2.2 is considered. This is because its derivation is more physically justified, and it gives generally better agreement with experiments (without modification to the equations).

The models for η mentioned above are still in use today. While they account for the advection of heat away from the wall, they do not consider modification to the heat flux due to 2D effects such as a reduction in the boundary layer temperature due to accumulation of coolant, and modification to the turbulent transfer of heat due to the coolant. These effects will be discussed in Chapter 5.

2.3 Numerical Modelling

Modern day computers can solve complex problems in relatively short periods of time, and this will only improve in years to come due to Moore's law. This has enabled the use of CFD as a design optimization tool [39]. By simulating fluid flow and heat transfer for a variety of design parameters, the number of physical parts that need to be tested in order to optimize a design can be reduced considerably. As an example, for the design of a re-entry vehicle, hypersonic flows with high-enthalpy are not easily reproduced in a lab setting. However, a computer can be used to simulate these high speeds, and can test many design parameters in order to optimize the design quickly and at low cost. The final geometries can then be tested experimentally to validate the simulations.

Transpiration cooling is a complex problem to model with CFD. This is in part due to the types of flows that the coolant interacts with, and in part because of the flow through

the porous media. The individual pores in the porous media are so small that they cannot be resolved for practical applications. Since the porous media is modelled with different equations than the hot gas flow, there must be a coupling of the two sets of CFD equations to obtain an accurate flowfield. Additionally, for space applications, the ideal coolant would be stored in liquid form and undergo a phase change to vapor somewhere within the transpiration cooling system, which further complicates the modelling. For re-entry vehicles, compressibility is a significant factor, which introduces modelling difficulties in the hot gas domain. For flows inside rocket engines, combustion processes must be modelled. Near the walls, the cooling of combustion gasses and the coolant species will affect the chemical reactions and hence the flowfield. The current state of CFD for modelling transpiration cooling will be discussed below.

Because of the small pore sizes which are not feasible to model for a practical application, most porous media solvers assume a homogeneous matrix, and assign macro-properties to the domain. Darcy's law for porous media can then be used to solve for conservation of momentum:

$$\epsilon u_i = -\frac{K}{\mu}\left[\frac{\partial p}{\partial x_i} - \rho g_i\right] \tag{2.5}$$

where K is the permeability of the porous medium, g is the gravity vector, u is the velocity vector, and ϵ is the porosity. Since K and ϵ are ill defined at a single point, local macro-properties are assigned for these values. Note that Darcy's law is only valid for low pore Reynolds numbers, and that modifications must be made for higher Reynolds numbers [40]. Darcy's law is well established in the field of porous media modelling. For the energy equations in porous media, generally at least the advection and conduction/diffusion of heat are considered for the fluid. As for the solid, the conduction is considered. If the heat transfer coefficient between the solid and fluid at a single point is high, then it is assumed that the solid and fluid are at equal temperatures at that point, and one energy equation is used. However, if the heat transfer is too low, then two energy equations are used, and they are coupled via a convective heat transfer term [32].

Modelling two-phase (liquid/vapor) flow in porous media becomes more difficult than modelling single phase flow. This is due to the additional physical phenomena that must be captured in the two-phase mixture region. For this case, there has been some development of models, particularly the Two-Phase Mixture Model (TPMM) [41], however there are still some convergence and discontinuity concerns with this model that must be addressed [42]. Work is being done to develop other two-phase models [43]. Since most space applications require coolant stored as liquid, development of this capability is important.

For the hot gas domain, RANS equations are typically used for practical applications of incompressible flow. For compressible flows, Favre-Averaged (i.e. density averaged) Navier-Stokes equations are often used. Closure of these equations requires modelling of the turbulence. One very successful model has been the SST model, which applies a two-equation k-omega model near the walls, combined with a two-equation k-epsilon model in the free stream [44]. While this model generally works well for a variety of applications, the turbulent structures near the wall may change with transpiration cooling. For this reason, Wilcox [18] suggests a modification for blowing walls. This modification is empirically derived, based on a limited set of experimental data. It is questionable whether this turbulence modification will work well for a wide range of transpiration cooling parameters.

In order to obtain accurate simulations of transpiration cooling systems, the models for both the porous media flow and hot gas flow domains must be coupled together. This is because the flow in one domain will affect the flow in the other. The coolant temperature and velocity leaving the porous domain will affect the fluid in the hot gas domain. Additionally, the interactions in the hot gas domain will affect the pressure and heat flux entering the porous domain. Therefore, the two domains are strongly dependant on each other.

Recently, there has been some work done to couple the two domains in transpiration cooling [19, 45]. Dahmen et al. [19] simulated air-in-air transpiration cooling by coupling a RANS solver with a porous media solver. They solve the system by using a weak formation for the porous media flow, and alternate between solving the porous media and RANS domains. At the interface, they prescribe a boundary condition that is updated at every iteration. The mass flux across the boundary is set based on experiment or the desired flowrate. Realistically, this mass flux would be an outcome of the pressure distribution, so this assumption may introduce error in a real situation. They validate their solver by comparing the simulated temperature and velocity distributions to those obtained in an experiment they performed.

Ding et al. [45] simulate the leading edge of a hypersonic vehicle with transpiration coolant injection via a coupled RANS and porous media flow solver. The boundary conditions are not described in much detail, however it is mentioned that each domain is added after the previous one has converged on a result with simpler boundary conditions, in order to promote fast convergence. Their simulations are compared to experiments for validation. Their results suggest that in regions where there is a higher heat flux (i.e. the leading edge of a hypersonic vehicle), the desired wall temperature can be obtained by modifying the porous media properties in order to locally increase the coolant mass flowrate.

The above coupled simulations assume that the coolant is injected uniformly. In reality,

the coolant is injected via discrete pores. For small pores it is likely that this uniform injection boundary condition has a negligible effect on the flow. However, with large pore sizes there may be effects that are non-negligible. The assumption of a uniform injection boundary condition will therefore be discussed in Chapter 5.

2.4 Direct Numerical Simulation

While modern day computers can be used to model flows, they can also be used to fully resolve flows via DNS. DNS is done by numerically solving the complete Navier-Stokes equations with sufficiently small grid spacing and time steps such that all relevant turbulent scales are fully resolved. Essentially, there is no modelling done in DNS, and therefore (if properly done) the results can be as accurate as experimental data. Many flows such as those at hypersonic speeds or at high temperatures are difficult not only to create experimentally in a lab, but also to measure with probes. DNS can be readily used to simulate these flows, and can give unique insights into the physics occurring. All relevant properties of the entire three-dimensional flow and thermal field can be obtained at every time step with DNS.

One of the challenges with using DNS in the past has been that it is very computationally expensive. This is due to the fact that the smallest scales in a turbulent flow require a very fine mesh, and because of this, the number of elements required scales at approximately $Re^{9/5}$ [46]. However, in recent years high-performance computers have been able to handle more complex DNS of turbulent flows. This has allowed researchers to study the fundamental physics in flows such as turbulent combustion [47], supersonic and hypersonic flows with heat transfer [48], and transpiration cooling. Since transpiration cooling can be a difficult system to test experimentally, DNS is uniquely suited to investigate the fundamental physical phenomena occurring.

One type of DNS simulation that has been performed to investigate the interaction between a turbulent boundary layer and a blowing wall is Couette/Poiseuille channel flows [49, 20, 21]. In these types of simulations, there is one blowing wall and one suction wall parallel to eachother. The boundary conditions for these walls are set such that there is equal mass flux and energy entering and leaving the domain. The flow is assumed to be periodic in the streamwise and spanwise directions (the flow at the outlet is recycled to the inlet of the domain). This creates a flow which is statistically stationary in the streamwise and spanwise directions (i.e. the mean properties only vary in the wall-normal direction).

Sumitani and Kasagi [49] performed DNS of a turbulent channel flow with suction and blowing at $Re_\tau = 150$, and a non-dimensional blowing velocity of $V_w/\mu_\tau = 0.05$ where

μ_τ is the friction velocity. They primarily investigated the turbulence, heat transfer, and skin friction. They found that the blowing wall decreased skin friction, but increased the turbulent activity, and therefore increased the turbulent stresses and turbulent transport of heat. The opposite effects were observed for the suction wall.

Avsarkisov et al. [20] have performed incompressible DNS of suction/blowing Poiseuille flows in the range of $Re_\tau = 250 - 850$, and blowing ratios (which is the mass flux ratio between the coolant and the freestream gas) in the range of $V_w/U_{bulk} = 0-0.05$, where U_{bulk} is the bulk velocity. They use these simulations to validate Lie symmetry analysis, and propose a new logarithmic velocity scaling law at moderate transpiration rates. Similarly, Kraheberger et al. [21] have performed DNS of Couette flow in the range of $Re_\tau = 250 - 1000$. Their work highlights the importance for the choice of scaling parameters, as their conclusions differ when applying an inner scaling using properties at the blowing wall versus using combined properties of the suction and blowing walls. This is due to the fact that increasing blowing velocity decreases u_τ, whereas the opposite is true for suction walls.

Another type of simulation that DNS is commonly used for is flow along a flat plate, and there have been some simulations of this flow incorporating a blowing wall [50, 22, 23]. In this type of flow, there is only one blowing wall, and the flow is only periodic in the spanwise direction. This type of flow, unlike the Couette/Poiseuille flows, is spatially developing. This allows for insights into how the gradual addition of coolant from the blowing wall effects the growing boundary layer. This spatial development is particularly important with regards to turbulence, drag, and heat transfer.

Kametani and Fukagata [50] simulated turbulent flat plates with blowing and suction walls using DNS. They used a $Re_\tau \approx 160$, and blowing ratios from 0% to 1%. Similar to channel flows, they found that blowing reduces skin friction, but increases turbulent activity. They found that the reduction in skin friction via blowing is due to the mean convection term in the decomposed skin friction coefficient equation. They also note that uniform blowing has a higher drag reduction efficiency compared to other types of active flow control considered.

Cerminara et al. [22, 23] have performed DNS of hypersonic laminar flat plates with transpiration coolant injection through holes and individual pores. They use a multiscale DNS approach, allowing them to simulate the flow through the individual pores. So far, this work has been primarily to prove that their approach to DNS can be used in these types of flows. The purpose of these simulations is to gain insight into the region where the coolant is injected into the boundary layer. For example, they have investigated the effect of plenum pressure and pore size on the velocity distribution along the plate. They have also investigated the effects of irregular pore geometry.

There has been a limited amount of transpiration DNS research in which heat transfer is a primary consideration. Most of the research in the past has been focused on drag reduction/control. For spatially developing turbulent boundary layers, there has been no DNS (to the author's knowledge) in which the fluid injected from the wall is colder than the hot gas flow. This is the gap in literature that the present work aims to address. By simulating this flow, a deeper understanding of the physical phenomena that effect turbulence and heat transfer can be obtained, and engineering models can be more easily derived and/or validated.

Chapter 3

Numerical Details

In this chapter, the numerical details of the simulations will be discussed. The DNS solver used in this work is HybridX, which was developed by Johan Larsson and Ivan Bermejo-Moreno [51]. It was chosen because it is accurate, fast, and scales well when run on a large number of CPU cores. Wall blowing conditions were added to the software as described in Section 3.1. In total, nine cases with transpiration cooling have been simulated, as well as a number of validation cases.

The Navier-Stokes equations completely describe the motion of viscous fluids through governing equation for conservation of mass, momentum, and energy. They are presented below in conservative form:

$$\frac{\partial \rho}{\partial t} + \frac{\partial (\rho u_j)}{\partial x_j} = 0 \tag{3.1}$$

$$\frac{\partial (\rho u_i)}{\partial t} + \frac{\partial (\rho u_i u_j + p\delta_{ij})}{\partial x_j} = \frac{\partial \sigma_{ij}}{\partial x_j} \tag{3.2}$$

$$\frac{\partial (\rho e)}{\partial t} + \frac{\partial [(\rho e + p) u_j]}{\partial x_j} = -\frac{\partial q_j}{\partial x_j} + \frac{\partial (\sigma_{ij} u_i)}{\partial x_j} \tag{3.3}$$

In the above equations, e is the total energy, σ_{ij} is the viscous stress tensor, and q_j is the heat flux vector. HybridX solves the compressible Navier-Stokes equations in conservative form with a skew-symmetric convective flux term. The spatial derivatives are approximated by a sixth-order central finite-difference scheme. High-order filtering is used to stabilize the spatial scheme [52]; in the vicinity of shocks or large density gradients, a Weighted Essentially Non-Oscillatory (WENO) scheme can be used (although it is not activated

given the subsonic nature of the present work). A fourth-order Runge-Kutta scheme is used for the time integration. The thermodynamic variables are related through the perfect gas law. A power-law function is used to account for temperature dependence on the variable viscosity of the fluid:

$$\mu = \mu_{ref}(T/T_{ref})^{0.75} \tag{3.4}$$

where μ_{ref} and T_{ref} are constant values set in the input file. This equation is used because it has a similar accuracy to Sutherland's law for the temperatures considered, but with a reduced computational cost. The simulations are run in non-dimensional units for increased computational efficiency. The fluid is the same for both the hot gas and coolant.

A schematic of the domain can be seen in Fig. 3.1. The Mach number in the freestream is set to 0.3 in order to minimize the effects of compressibility. The Prandtl number is fixed at 0.7. Based on a unitary inlet boundary layer thickness ($\delta_i = 1$), the non-dimensional domain size is $Lx = 60$, $Ly = 6$, $Lz = 6$. For reference, this corresponds to $\delta_i \approx 2mm$ for the cases with transpiration cooling (taking air at a freestream temperature of $800K$).

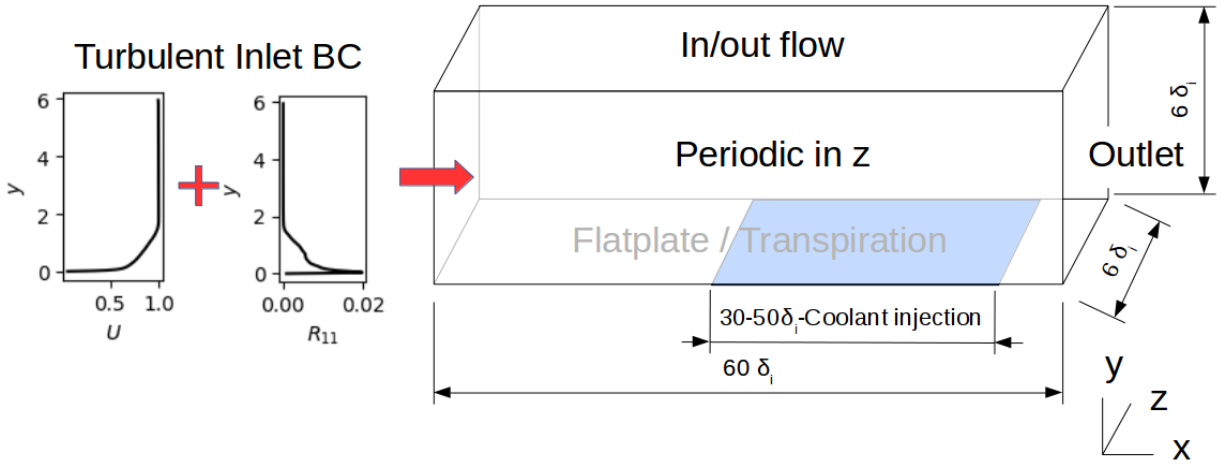

Figure 3.1: Computational domain with representative inflow boundary layer characteristics.

3.1 Boundary conditions

For the inlet, the average velocities and Reynolds stresses were taken from a well-established direct numerical simulation of an incompressible turbulent boundary layer at $Re_\tau = 450$ [53]. Randomly generated turbulence with the desired Reynolds stress profiles is superimposed on the desired mean flow profiles at the inlet plane. Digital filtering, in both space and time, assures a more realistic correlation length of the turbulent fluctuations. At the top and outlet of the domain, in/outflow boundaries are specified which use a Summation-By-Parts (SBP) scheme with a Simultaneous Approximation Term (SAT) penalty to compute the fluxes. Sponge layers are applied to the outlet boundary in order to dampen numerical reflections/fluctuations in the flowfield properties. The domain is periodic in the z direction.

For the transpiration-wall modelling, no-slip conditions have been applied in the x and z directions. In the y direction, the wall-normal velocity is set depending on the case. The fluid is the same for both the hot gas and coolant. It is assumed that the coolant is injected in a laminar state. This is often the case, due to very small pore channels resulting in low pore Reynolds numbers. Two different treatments for the velocity profile of the injected coolant have been used in this study. The first is a constant velocity over the transpiration region, which will be denoted as uniform blowing. The second is a parabolic profile which would be observed in a laminar channel flow, with the wall-normal velocity varying in the streamwise direction only. This profile is then repeated multiple times over the transpiration region. These spanwise-aligned slits are separated by regions of impermeable, no-slip walls. This second profile is denoted as slit blowing, since it models blowing of coolant from multiple slits. A visual representation of the transpiration wall boundary conditions (BC) is shown in Fig. 3.2.

At the blowing boundary, the temperature is prescribed, the pressure is taken from the flow domain, and the density is computed to satisfy the perfect gas law. These wall values, along with the velocity at the wall, are used to compute the inviscid and viscous flux boundary conditions. Because of this condition, there is a slight difference in the density, and therefore mass flux, of the coolant injected from the leading to trailing edge of the transpiration region. This is due to the slight pressure gradient on the plate that is induced by the injection of coolant. However, this difference is small, and therefore is not considered significant (it is on the order of 1% for the highest blowing ratio).

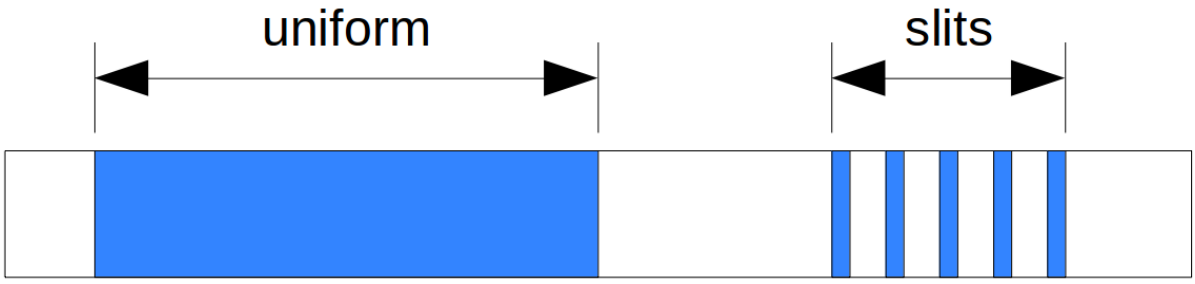

Figure 3.2: Transpiration BCs (top view). Blue represents regions where $v \neq 0$, white an impermeable wall ($v = 0$).

3.2 Simulated Cases

In total, 4 uniform blowing cases, 5 slit blowing cases, and 2 reference cases with no blowing were simulated. The simulations that are discussed in Ch. 5 are summarized in Tab. 3.1. Additional validation cases were also run, which will be described in Ch. 4. For the reference simulations, both an adiabatic and an isothermal case were simulated in order to validate the results against established data from the literature. The adiabatic case will not be discussed in detail, however it should be noted that the results are in good agreement with the data from Jiménez et al. [53]. For the isothermal simulation, at the center of the domain (x=30), the Reynolds numbers are: $Re_\tau = 600$, $Re^*_\tau = 260$, $Re_\theta = 790$, $Re_{\delta 2} = 1320$. At the same location, the non-dimensional wall heat transfer rate is $B_q = \overline{q}_w/(\overline{\rho}_w C_p u_\tau \overline{T}_w) = 0.043$.

The differences between the cases are highlighted in Tab. 3.1. For all cases in Tab. 3.1, a cooled, isothermal wall boundary condition of $T_w/T_\infty = 0.5$ is used. The coolant is injected at the same temperature as the wall ($T_c = T_w$). The subscripts ∞, c, and w correspond to the freestream, coolant gas at injection, and wall quantities, respectively. For all of the isothermal simulations, $\mu_{ref} = 0.000147$ and $T_{ref} = 0.5$. The blowing ratio is defined as $F = \overline{\rho}_c \mathbf{V}_c/\overline{\rho}_\infty U_\infty$, where $\mathbf{V}$ is the average Darcy velocity. In mathematical terms

$$\mathbf{V} = \frac{1}{x_b - x_a} \int_{x_a}^{x_b} V dx,$$

where x_a and x_b are the beginning and end of the transpiration region ($x_a = 30$ and $x_b = 49.6$ for all cases unless otherwise stated). For all the slit simulations, the ratio of blowing area to total wall area (*i.e.* the wall porosity) is 1/3, thus the maximum local blowing velocity for each slit keeps constant, independent of the slit size.

Simulations	F	Notes
Flatplate2	0	
Uniform-2%-1	0.02	
Uniform-2%-2	0.02	injection from $x_a = 30$ to $x_b = 40$
Uniform-0.6%	0.006	
Uniform-0.2%	0.002	
Slits-2%-1	0.02	28 slits, width of $0.234\delta_i$ each
Slits-2%-2	0.02	14 slits, width of $0.469\delta_i$ each
Slits-0.6%-0.5	0.006	57 slits, width of $0.117\delta_i$; $x_b = 50$
Slits-0.6%-1	0.006	28 slits, width of $0.234\delta_i$ each
Slits-0.6%-2	0.006	14 slits, width of $0.469\delta_i$ each

Table 3.1: Details of the DNS cases.

For all cases in Tab. 3.1, the mesh is the same. The mesh is fully structured, with a wall-normal grid clustering. The number of grid points is ≈ 118 million with $2560 \times 180 \times 256$ points respectively in the x, y, and z directions. Validation for this grid and other parameters of the simulation are discussed in Ch 4. A temperature snapshot of the Uniform-2%-1 case is shown in Fig. 3.3, in order to give the reader a visualization of the flow.

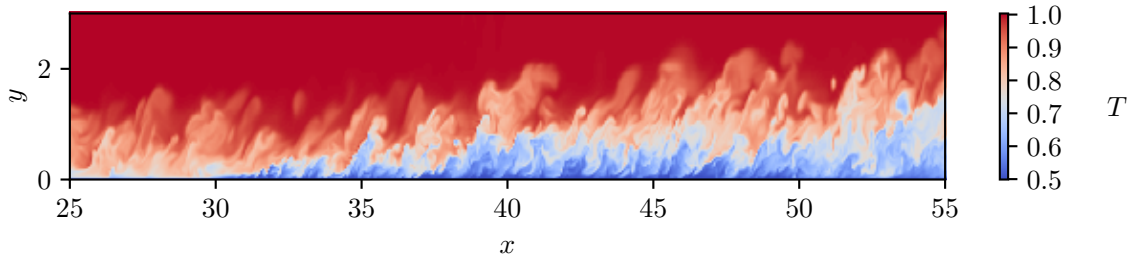

Figure 3.3: Instantaneous temperature snapshot, Uniform-2%-1 simulation. Coolant is injected from $x = 30$ to $x = 50$.

Chapter 4

Validation

In this chapter, analysis on the validity of the simulations, and uncertainty in the results, are discussed. First, the baseline flat plate simulation without coolant is compared to data from literature in Sec 4.1. It is found that there is good agreement between the present simulations and other literature. Next, the effect of the mesh resolution is investigated in Sec 4.2. The differences due to the mesh are deemed acceptable for the analysis done in this work. The effects of the upper boundary are also discussed in Sec 4.3, and found to have a negligible effect. Finally, the length of the simulation and the averaging window are discussed in Sec 4.4 to ensure that the results are statistically stationary. Sampling uncertainty has been calculated in Appendix A, and found to be negligible. The analysis in this chapter shows that the simulations are of sufficient accuracy for the present work.

4.1 Comparison to other works

One common validation technique for DNS is to compare the results to the known law of the wall after scaling the data. For incompressible flows, the average streamwise velocity and height are non-dimensionalized by the corresponding characteristic velocity and length scales at the wall. The velocity scale is the friction velocity $u_\tau = \sqrt{\overline{\tau}_w/\overline{\rho}_w}$, and the length scale is the viscous length scale $l_\nu = \overline{\mu}_w/(\overline{\rho}_w u_\tau)$. The velocity scaled by inner units is therefore $U_I^+ = U/u_\tau$, and similarly $y_I^+ = y/l_\nu$.

Since the flows simulated here incorporate compressibility, using an incompressible scaling will lead to error. Van Driest derived a correction to the incompressible scaling in order to apply it to compressible boundary layers [54]. While this formulation has been shown

to work well in simple cases with adiabatic walls, it breaks down in flows with large thermophysical property variations such as walls with high heat transfer [55]. For these cases, there have been multiple corrections which have been proposed [56]. The transformation that is chosen for the present data was developed by Trettel and Larsson [55]. This scaling is derived by applying a correction to the Van Driest transformation that more accurately scales the viscous stresses. The scaling is:

$$y^+ = \frac{\overline{\rho}(\overline{\tau}_w/\overline{\rho})^{1/2} y}{\overline{\mu}} \tag{4.1}$$

$$U^+ = \int_0^{U_I^+} \left(\frac{\overline{\rho}}{\overline{\rho}_w}\right)^{1/2} \left[1 + \frac{1}{2\overline{\rho}}\frac{d\overline{\rho}}{dy} y - \frac{1}{\overline{\mu}}\frac{d\overline{\mu}}{dy} y\right] dU_I^+ = \int_0^{U_I^+} \left(\frac{\overline{\mu}}{\overline{\mu}_w}\right) \frac{dy^+}{dy_I^+} dU_I^+ \tag{4.2}$$

Trettel and Larsson [55] have shown that this scaling works well for compressible flows with heat transfer. There are still some discrepancies using this scaling for hypersonic flows [48]. This may be due to the weakness of the arguments in the buffer layer, the invalidity of Morkovin's scaling, and/or the additional stress terms that may be non-negligible for hypersonic flows.

For scaling the turbulent intensities $u'_{i,rms} = \sqrt{\overline{u'_i u'_i}}$, Trettel and Larson [55] suggest, through their derivation, that Morkovin's scaling [57] should be used. This scaling is:

$${u'_{i,rms}}^+ = \sqrt{\frac{\overline{\rho}}{\rho_w}} \frac{u'_{i,rms}}{u_\tau} \tag{4.3}$$

This transformation has also been shown to better collapse compressible data compared to scaling with only u_τ [58].

For the baseline comparative case without injected coolant (Flatplate2), the wall-normal resolution at $x = 30$ (*i.e.* the center of the domain) is $y_w^+ \approx 1$ with $\triangle y^+|_{\delta_{99}} \approx 6$, while the maximum streamwise and spanwise resolution is $\triangle x^+ = \triangle z^+ \approx 11$. Compared to other works [58, 15], this resolution appears reasonable. Additional validation has been done on the mesh resolution in Section 4.2

In order to validate the simulation setup, the isothermal reference case (Flatplate2) is compared to results in literature. Since no other DNS data for low Mach number compressible flows with heat transfer were found, the results are compared to incompressible adiabatic turbulent flat-plate data from Jiménez et al. [53]. The data from Jiménez et al. [53] is chosen due to its comparable Reynolds numbers to the Flatplate2 case, which minimizes the minor effects of the Reynolds number on the U^+ vs y^+ profile in the inner

layer [55]. Using the transformed values of U^+ and y^+, the adiabatic incompressible data and the compressible case with heat transfer should yield the same results in the inner region of the boundary layer [55] (assuming the simulation is accurate).

The comparison between the Flatplate2 case and the data from literature [53] can be seen in Fig. 4.1. Figure 4.1(a) shows that with the proper scaling applied to the data, the results collapse in the inner layer. When the Van Driest transformation is applied instead (not shown here), the scaling does not match the adiabatic incompressible data. Figure 4.1(b) compares the turbulent intensities in the inner layer of the Flatplate2 simulation to reference incompressible adiabatic data. While the results generally agree, there is a higher peak in the streamwise turbulence intensity for the present data. At least part of the discrepancy can be accounted to mesh resolution. The effect of mesh resolution on this peak is further discussed in Section 4.2. Part of the reason for this discrepancy could also be that the comparison data is adiabatic. It has been shown by other works that this peak does increase for supersonic and hypersonic compressible flows with heat transfer to the walls [59, 48]. As previously mentioned, no other DNS of a subsonic compressible

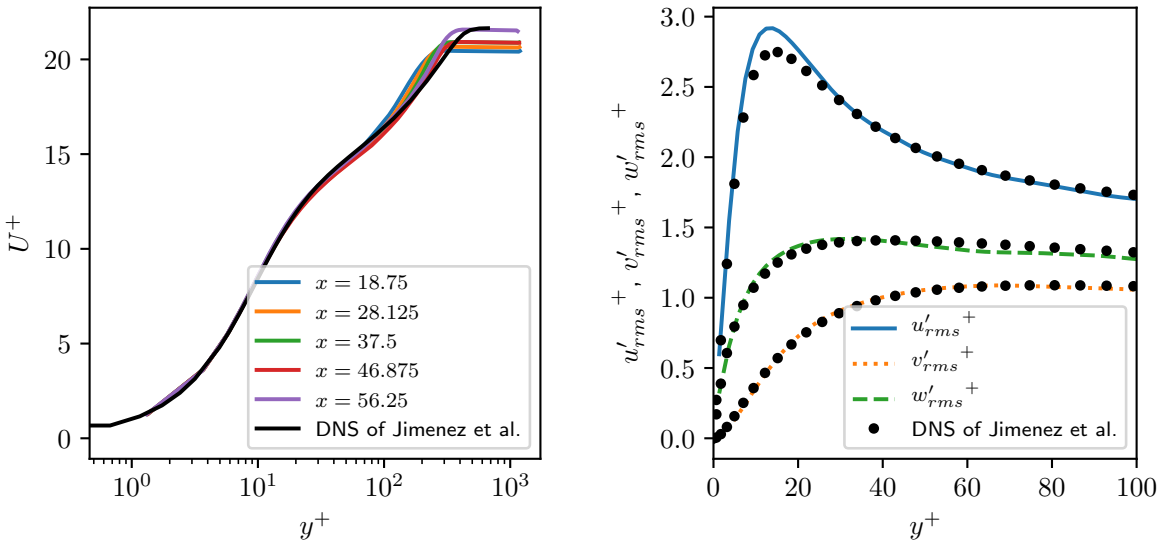

(a) Law of the wall scaling

(b) Turbulent intensities at x = 46.875

Figure 4.1: Cooled flatplate simulation (Flatplate2), compared to incompressible adiabatic flatplate DNS from Jiménez et al. [53] at $Re_\tau = 450$.

turbulent flat-plate flow with heat transfer was found in the review of literature. For the purpose of this work, the agreement of the present data to other DNS data in literature is acceptable.

4.2 Mesh resolution study

A grid convergence study was undertaken to assess the adequacy of the selected resolution. The Flatplate2 simulation was re-run with the mesh resolution doubled in the z direction (to 512 points), since the z resolution is often chosen to be double that of the x resolution [58, 15]. Additionally, a simulation was performed in which the resolution in x, y, and z were all doubled (to $5120 \times 360 \times 512$ points $\approx$ 944 million grid points). Since the higher resolution computation was more expensive, it was initialized from the output of the baseline resolution simulation, and was allowed to settle for only a fraction of the largest eddy turnover time. The results are shown in Fig. 4.2. The results generally agree, however there is more variance in the higher resolution mesh case. This is likely due to large eddies effecting the averaging window (as will be discussed in Sec 4.4). The difference in total wall heat flux within the region between $x = 30$ and $x = 50$ is less than 1% between the reference case and the case with double the mesh resolution. This difference is acceptable in the context of the present research.

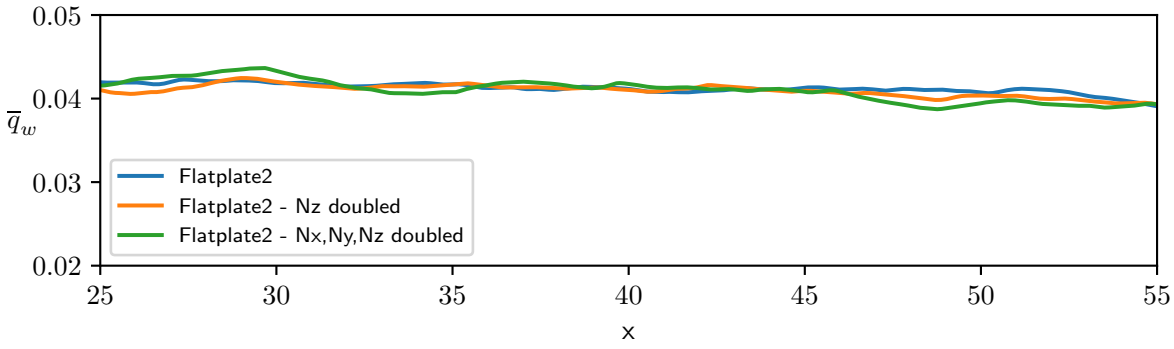

Figure 4.2: Heat flux comparison for mesh resolution study

In addition to the analysis on the wall heat flux, the average peak in ${u'_{rms}}^+$ between $x = 30$ and $x = 50$ was also considered. The values are summarized in Tab. 4.1. It

was found that the peak did decrease with increased mesh resolution, however it is a more sensitive quantity than wall heat flux. There may also be some variance in this value due to the averaging window. Small differences in the peak ${u'_{rms}}^+$ are not critical for the analysis and key results in this work. Therefore, it was deemed that the additional computational expense for the higher mesh resolution was not justified.

Simulations	Flatplate2	Flatplate2 - Nz doubled	Flatplate2 - Nx,Ny,Nz doubled
${u'_{rms}}^+$ peak	2.88	2.85	2.82

Table 4.1: ${u'_{rms}}^+$ peak for different mesh resolutions

4.3 Effect of upper boundary

The upper boundary of the simulation was an area of concern due to the wall normal velocity field. A domain that is too small in the wall normal direction could effect the flow in the boundary layer, and reflections at this boundary could also cause issues. In order to address these concerns, the Uniform-2%-1 simulation was re-run with two variations on the upper boundary. This simulation was chosen because it has the highest blowing rate, and therefore it is expected to be the case that is the most sensitive to the upper boundary. The first variation of the simulation was to double the domain height (to $Ly = 12$). The grid spacing in y was the same as the baseline case near the wall. Farther away from the wall, the resolution was slightly higher for a given height (due to the mesh biasing algorithm). There were 300 points in y for the case with double the domain height, as compared to 180 for the baseline case. In addition, a simulation with a sponge layer applied to the top boundary was performed. The sponge layers began at $y = 5$, and are intended to prevent spurious oscillations. The top sponge layers were intended for all the simulations, however a mistake in the input file identified later showed that the sponge layers were not applied (they were only applied at the outlet). Therefore, analysis is done here to ensure that this does not considerably affect the flow field. The statistic chosen to compare the simulations was the average cooling effectiveness, and is shown in Fig. 4.3. The differences are within the uncertainty caused by the averaging window (as will be discussed in Sec 4.4). Therefore, it is concluded that the choice of upper boundary height, and the omission of sponge layers for the upper boundary are acceptable.

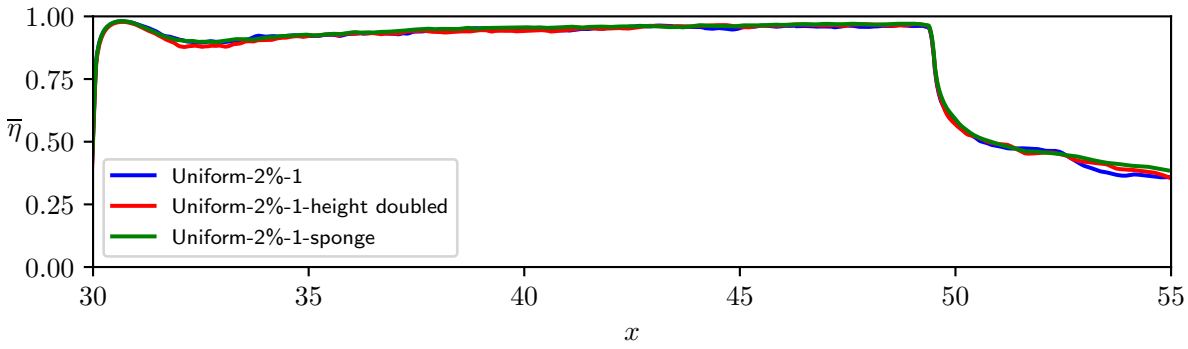

Figure 4.3: Cooling effectiveness comparison for the Uniform-2%-1 case with different upper boundaries

4.4 Time convergence study

Time convergence in DNS pertains to running the simulation for long enough that the results are statistically stationary. A rule of thumb for this is to discard two times the turnover time for the largest eddies, which is approximated by δ_{99}/u_τ [53]. After this time, the statistics can be calculated. In order to be conservative, a minimum of four eddy turnover times were discarded. Additionally, it is important to compute the averages over a period which is long enough that the effects of the largest/slowest eddies are smoothed out of the statistics. Again, this can be compared to δ_{99}/u_τ. The data has been averaged for 1-2 eddy turnover times, as well as being averaged in the z direction. For reference, Zhang [48] used 1.4 - 14.9 eddy turnover times, and Jimenez [53] used 21 eddy turnover times in order to compute statistics. The papers mentioned above focus on higher-order statistics, which are more sensitive to the statistical sample size. While a longer averaging time would be preferred, the computational expense was determined to be too high. Instead, additional analysis was done in order to determine the effect of the smaller averaging window.

To determine if the simulation has reached a steady state, and to analyze the averaging window, one of the simulations (Uniform-0.6%) was run for longer than the others, and the values of the wall shear stress and wall heat flux are analyzed. While the simulation is running, some values are computed at the wall near the end of the domain (but before the outlet sponge layers) at every time instance, as shown in Fig. 4.4. In order to be consistent in terms of sampling uncertainty, a 13,000 point moving average has been applied (which

corresponds to an averaging window of roughly δ_{99}/u_τ). This simulation was initialized from the output of the Uniform-0.2% case, which is why it appears to already begin from a reasonable solution. Some low frequency variation is observed in the moving average. Applying similar analysis to Appendix A, the standard error in the mean wall heat flux is $SE_{q_w} \approx \pm 0.00002$, which is effectively negligible. The standard error in the wall shear stress is similarly negligible. However, the standard deviation of the mean computed from Fig. 4.4 is on the order of 2%. The variance in the mean observed is due to large scale structures in the flow. Since an averaging period corresponding to only one large eddy turnover time was used, some eddies may reside for a significant portion of the averaging period. A larger averaging window could be used to smooth out this variation. The above analysis was for a single location averaged in time, but the averages computed for the other analyses was also averaged spatially in z. This is expected to lower the variance on the mean.

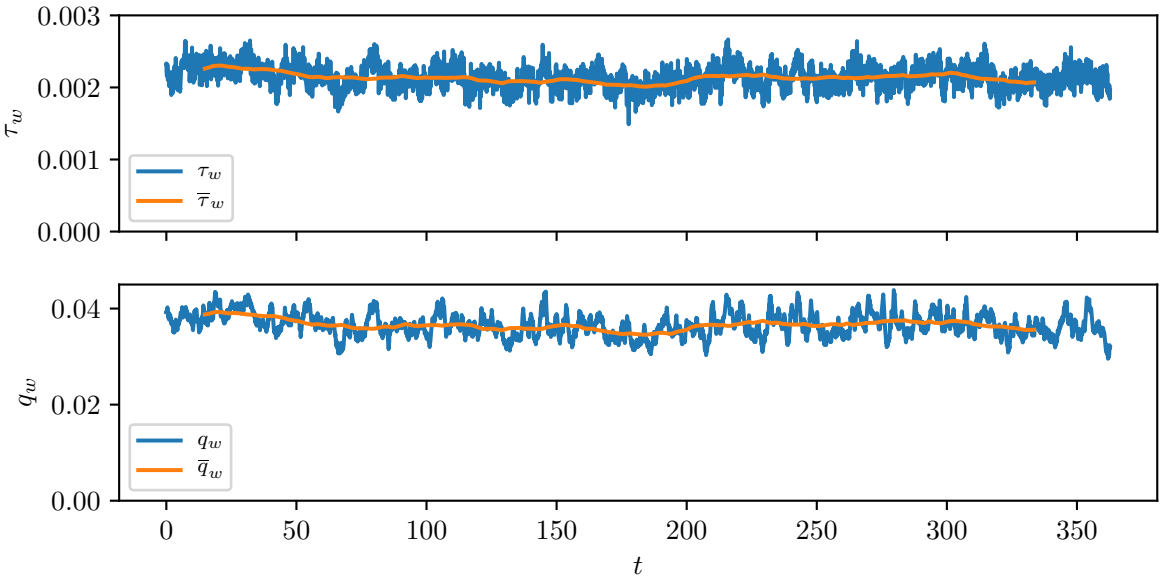

Figure 4.4: Wall heat flux and shear versus time, Uniform-0.6% simulation

To further validate the simulations, the averages for the Uniform-0.6% were computed over a period of two eddy turnover times beginning at the time in which it was assumed that the Uniform-0.6% simulation had converged according to the above analysis, and this

was compared to averages beginning at later times. The comparison is shown in Fig. 4.5. While the results generally show good agreement, there is some noticeable deviation, particularly in the region immediately after the transpiration. The likely explanation for this discrepancy is again the periodic shedding of some larger vortices, which may cause low frequency deviations in the flow properties. By taking the difference between the averaged results, the standard deviation in the mean from $x = 30$ to $x = 50$ was calculated as 2%. For the purpose of this work, this level of uncertainty is deemed sufficient.

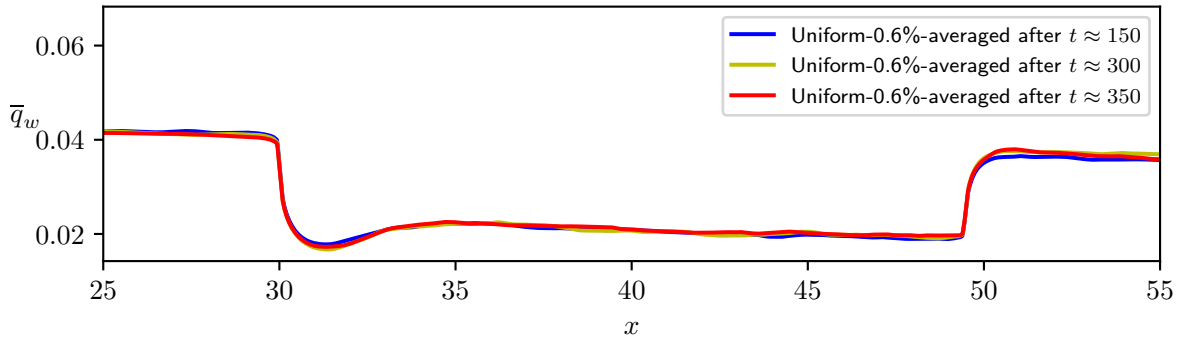

Figure 4.5: Heat flux comparison for the Uniform-0.6% case with different averaging periods

Chapter 5

Results and Discussion

In this chapter, the physics of transpiration cooling are discussed using the results of the DNS data. First, the effect of the blowing ratio on the turbulence intensity is discussed in Sec 5.1. Following this, physical phenomena influencing the cooling effectiveness are discussed in Sec 5.2, and a model to account for the accumulation of coolant is derived and shown to agree well with the data. The law of the wall for transpiration cooling is analyzed in Sec 5.3, and reasons for the failing of classical scalings at high blowing ratios are discussed. In a real transpiration cooling system the coolant is injected through individual pores, whereas the modelling assumption of a uniform injection boundary condition is often made in simulations. This assumption is discussed by comparing the results of the slits simulations to the uniform blowing simulations in Sec 5.4. Finally, the increase in vortical structures in the flow due to the injection of coolant, and their effect on heat transfer, are discussed in Sec 5.5.

5.1 Effect of Blowing Ratio on Turbulence

In this section, the turbulence at three different blowing ratios with uniform injection are compared (*i.e.* Uniform-2%-1, Uniform-0.6%, and Uniform-0.2%). The modification of turbulent kinetic energy (TKE) can be used to quantify the effect of the blowing ratio on the turbulence. The TKE is defined as:

$$k = \frac{1}{2}(\overline{u'u'} + \overline{v'v'} + \overline{w'w'}) \tag{5.1}$$

The time and spanwise averaged TKE for the three blowing rates is shown in Fig. 5.1. It can be seen that for the lowest blowing ratio (Uniform-0.2%), the TKE remains relatively unchanged in structure and magnitude within the region where coolant is injected. For the medium blowing ratio (Uniform-0.6%), there is more turbulence produced in the transpiration region, however it appears that the peak turbulence production is still near the wall. For the high blowing ratio (Uniform-2%-1) the TKE is greatly enhanced away from the wall, but close to the wall the turbulence is reduced.

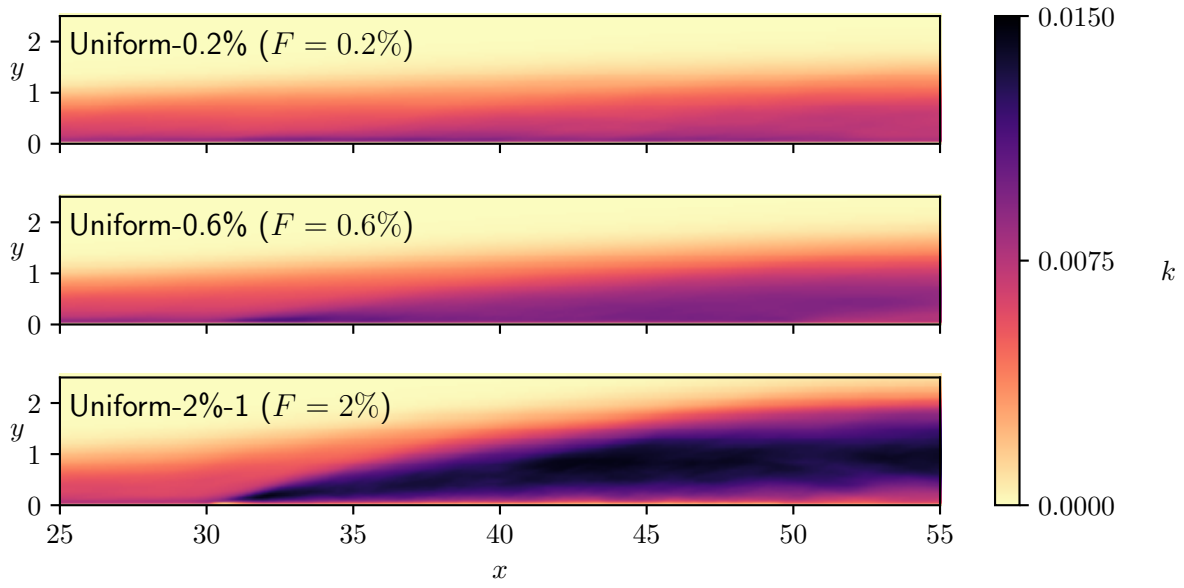

Figure 5.1: Average turbulent kinetic energy at different blowing rates

In order to discuss the mechanism of turbulence modification, the interface between the coolant and hot gas is identified. This is done using automatic interface identification based on a Fuzzy C-means algorithm (see details in [60]). Recently, this method has been applied to identify Uniform Momentum Zones (UMZ) [60], as well as Uniform Thermal Zones (UTZ) in transcritical flows [61]. In Fig 5.2, three clusters have been applied to the x-y plane snapshots of the temperature field in order to identify the three zones. These zones correspond to the coolant gas layer, the hot gas boundary layer, and the freestream. The interface of interest corresponds to the delineation between the first two zones. The computed interfaces were averaged together to obtain the average interface location. It can be seen that for the Uniform-0.2% case, the interface between the coolant and hot gas

is very close to the wall. For the Uniform-0.6% case, this interface moves away from the wall slightly. For the Uniform-2%-1 case, the interface is significantly pushed away from the wall (to roughly half the boundary layer height).

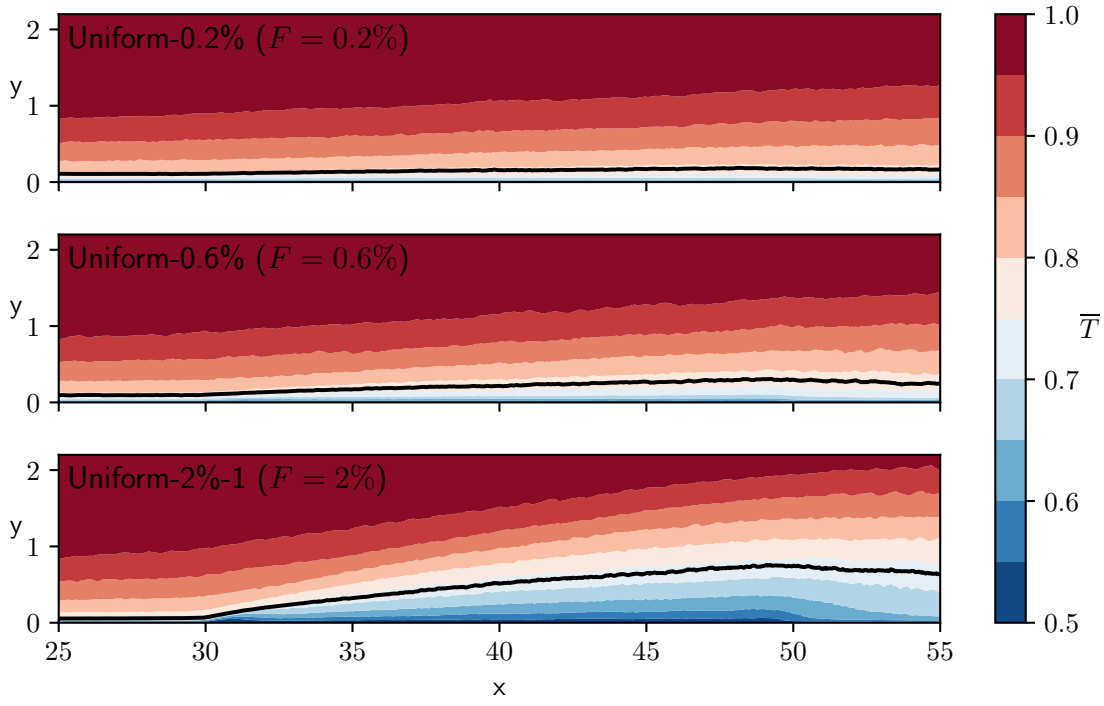

Figure 5.2: Interface identification for different blowing rates. The contours correspond to the time and spanwise averaged temperature. The black line indicates the location of the averaged interface between the hot gas boundary layer and coolant gas layer.

The near-wall coolant gas has a low momentum compared to the deflected hot-gas boundary-layer flow, and their interaction is accompanied by a shear layer at the interface. This causes an increase in the turbulence production away from the wall. For the Uniform-2%-1 case, the shear between the hot gas and coolant dominates, creating a peak in the turbulence production away from the wall. The coolant layer and shear interaction also act to protect the wall from the hot gas flow. This results in a decrease of the turbulence production peak close to the wall. In a sense, the incoming hot gas boundary layer has separated from the wall in the Uniform-2%-1 case due to the large amount of coolant pushing against it.

To supplement the TKE plots, the diagonal components of the Reynolds stress tensor are shown in Fig. 5.3 at $x = 40$ (in the transpiration region) and at $x = 55$ (after the transpiration region). In order to compare the data in a meaningful way, no (inner) scaling has been applied for these plots. This is because the wall shear stress decreases with increasing blowing rate, and therefore applying a scaling would artificially show that a higher blowing ratio has higher normalized Reynolds-stress components (which is not physically insightful).

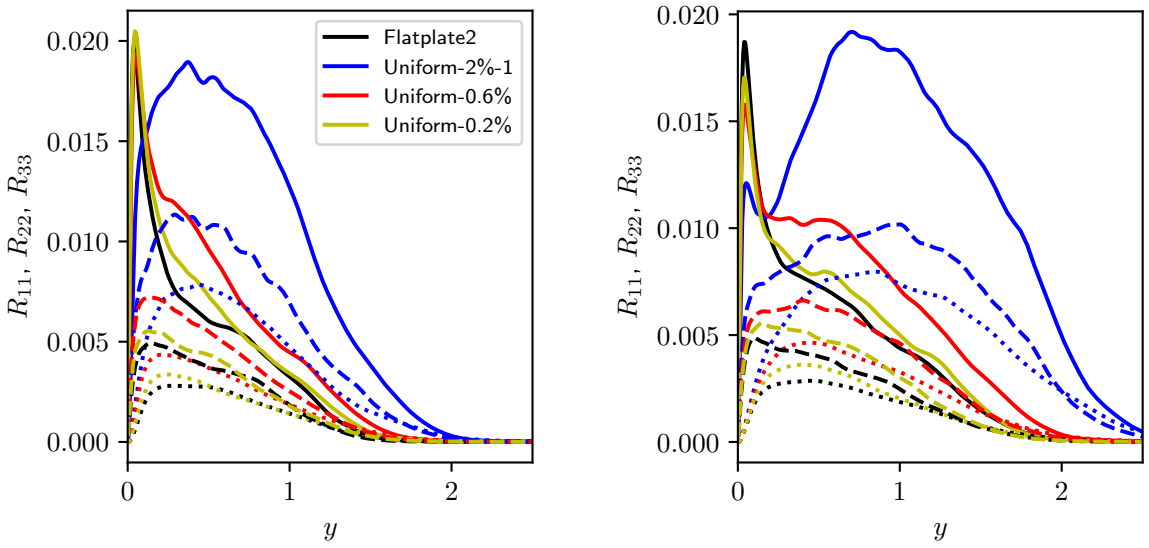

(a) x=40

(b) x=55

Figure 5.3: Reynolds stresses vs y. R_{11} —— ; R_{22} ····· ; R_{33} ---- .

Figure 5.3 shows that inside the transpiration zone the highest blowing ratio no longer retains its peak in R_{11} near the wall. Instead, the TKE maximum is pushed away from the wall. This is consistent with the argument that the coolant has pushed the incoming hot gas boundary layer away from the wall. Downstream of the transpiration, a peak in R_{11} close to the wall begins to grow again. This is because there is no wall-normal velocity in this region to prevent the boundary layer from approaching the wall. Therefore, the flow begins to re-attach to the wall. In the lower blowing-ratio cases, the R_{11} stress is increased in the outer region of the boundary layer, however the peak close to the wall does not increase - it actually decreases downstream. In these cases, the hot gas flow is still attached to the wall.

However, as the coolant enters the boundary layer, it still creates shear as it interacts with the hot gas. This shear produces vortices that cause velocity fluctuations in all directions, resulting in an increase in all the Reynolds stresses (notice that R_{22} and R_{33} stresses also increase in comparison to the reference case). The decrease in R_{11} downstream as shown in Fig. 5.3(b) is primarily due to the increased thickness of the boundary layer caused by the addition of coolant. However, the increased shear away from the wall may also slow the hot gas down as it approaches the wall, which may further reduce the wall shear.

5.2 Cooling Effectiveness

Transpiration cooling will reduce the heat flux being transferred into a porous media. Analytically, the heat flux going into a wall can be described by:

$$\overline{q}_w = h(\overline{T}_{w,ad} - \overline{T}_w) \tag{5.2}$$

where h is the heat transfer coefficient, T_w is the wall temperature, and $T_{w,ad}$ is the temperature at the wall in the adiabatic case. In an adiabatic incompressible flatplate case, $\overline{T}_{w,ad} = \overline{T}_\infty$ (the free-stream temperature of the main flow). However, when film or transpiration cooling is added, $\overline{T}_{w,ad}$ changes. This change can be described in terms of the effectiveness of the cooling method:

$$\overline{\eta} = (\overline{T}_\infty - \overline{T}_{w,ad})/(\overline{T}_\infty - \overline{T}_c) \tag{5.3}$$

It can be seen that at $\overline{\eta} = 1$, $\overline{T}_{w,ad} = \overline{T}_c$, in which case the coolant would completely insulate the wall from the free stream. At $\overline{\eta} = 0$, $\overline{T}_{w,ad} = \overline{T}_\infty$, in which case no insulating effect would be observed. Therefore, by deriving a relationship for $\overline{\eta}$, and also determining h, it is possible to predict the heat flux into the solid material. For high speed flows, the recovery temperature of the free stream must also be considered. Since in the present case the Mach number is low, this is not a concern.

In the choice of boundary condition, $T_w = T_c$ has been prescribed. Therefore, Equation 5.2 can be substituted into Equation 5.3 to obtain:

$$\overline{q}_w = h(1 - \overline{\eta})(\overline{T}_\infty - \overline{T}_w) = \overline{\lambda}\frac{d\overline{T}}{dy}\bigg|_w \tag{5.4}$$

5.2.1 Advection model

In the transpiration zone, there is advection of heat away from the wall due to the non-zero value of V at the wall. To show that this advection effect is important, average temperature profiles and the advection term $\overline{\rho}V C_p \partial\overline{T}/\partial y$ are plotted for the Slits-2%-2 case between the jets, and at a jet center (in Fig. 5.4). Between the jets, V_w is zero. however, inside the jet, the wall normal velocity is large, causing advection of heat away from the wall. In the outer portion of the boundary layer, turbulence dominates the heat transfer, and so there is minimal effects of the jet advection on the temperature. It is only close to the wall where there is a lack of turbulence that this advection term is dominating. It can be seen that at the wall, this advection creates a very large difference in the gradient of $\overline{T}$, and therefore in the wall heat flux. Inside the jet, the temperature gradient at the wall is effectively zero. There may be other 2D/3D effects in the jet case that also modify the energy equation. For example, the pressure/velocity fields may cause there to be some advection even between the jets.

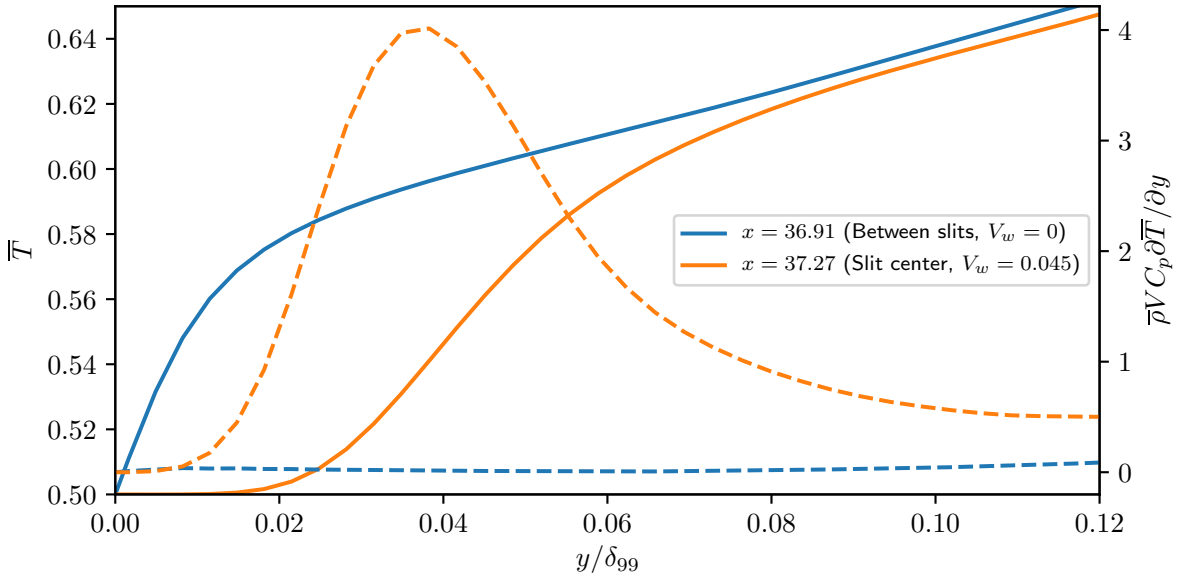

Figure 5.4: Effect of advection on heat transfer, Slits-2%-2 case. ---- advection term ; —— average temperature

In an attempt to account for the effect of heat advection, several models were proposed over 50 years ago. The derivations are primarily based on a simplification of the energy equation. Further detail on the models can be found in Sec. 2.2. The cooling effectiveness due to advection may be modelled as:

$$\overline{\eta}_{advect} = 1 - \frac{r\varphi}{e^{r\varphi} - 1} \tag{5.5}$$

Figure 5.5 compares the cooling effectiveness obtained from the DNS data to the predicted effectiveness according to Eq. 5.5 (triangle symbols). In the transpiration region this model works reasonably well. However, in the post-transpiration region this model predicts $\overline{\eta} = 0$. This is because the model only accounts for the reduction of heat due to advection at the wall, and in regions where there is no transpiration at the wall, the advection is zero.

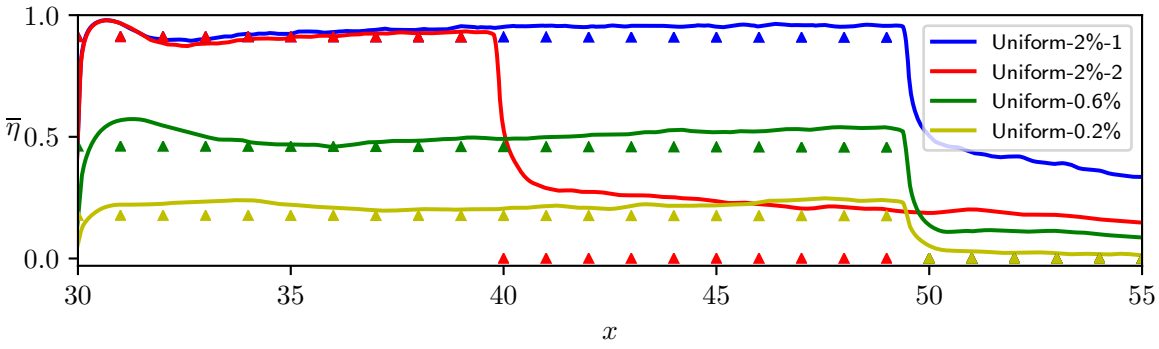

Figure 5.5: Cooling effectiveness. solid: DNS data ; triangles: advection model (Eq. 5.5)

There is another cooling mechanism, which is the reduction of heat transfer to the wall caused by the accumulation of coolant. The coolant effectively reduces the temperature of the near-wall boundary-layer region, and therefore reduces the transfer of heat to the wall. In order to account for this effect, another model must be incorporated. This additional model is derived in Section 5.2.2, and combined with Eq. 5.5 in Section 5.2.3.

Other minor differences in Fig 5.5 are observed. Near the end of the transpiration region, the effectiveness rises slightly, and the model under-predicts the cooling effectiveness. This may also be explained by the accumulation of coolant. Near the leading edge of

the transpiration region, there is a peak in the cooling effectiveness. This phenomenon is associated with the turbulent transport of heat, and will be discussed further in Section 5.5.

5.2.2 Film accumulation model

As mentioned previously, the gradual addition of coolant into the boundary layer will lower the average boundary layer temperature, therefore lowering the adiabatic wall temperature. This effectively lowers the amount of heat flux entering the wall. To show that this is the case, average temperature profiles at various x locations have been plotted in Fig. 5.6. It is evident that as more coolant is injected, the average temperature of the boundary layer decreases.

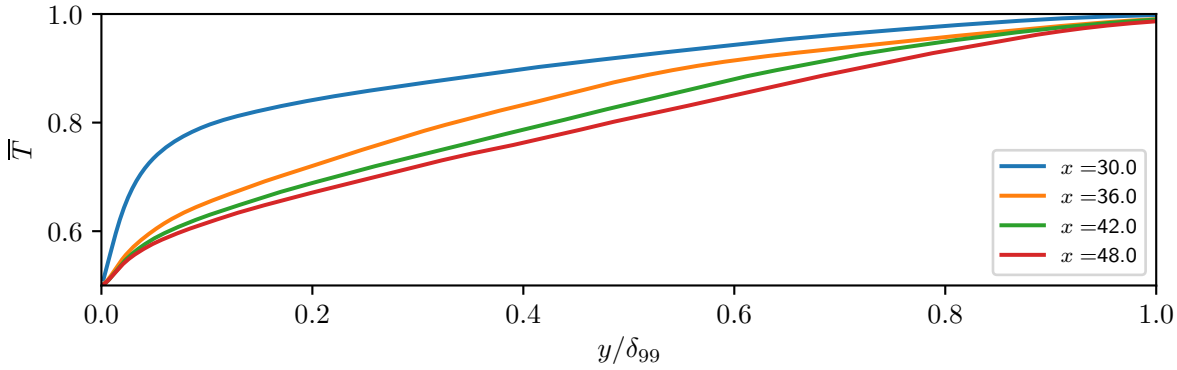

Figure 5.6: Average temperature profile at various x locations, Uniform-2%-1 case. The transpiration region lies between $x = 30$ and $x = 50$.

One very successful model in predicting η for film cooling focuses on the energy balance in the boundary layer [26]. It is assumed that the heat transfer is reduced only due to the lowering of the boundary-layer temperature because of the accumulation of coolant. For gas-in-gas cooling, assuming that $\langle T \rangle \approx T_{w,ad}$ (where $\langle T \rangle$ is the average boundary layer temperature, and $T_{w,ad}$ is the adiabatic wall temperature), the cooling effectiveness can be modelled as [26]:

$$\overline{\eta}_{film} = \frac{1}{1 + \frac{\dot{m}_\infty C_{p,\infty}}{\dot{m}_c C_{p,c}}} \tag{5.6}$$

The main unknown in this model is the ratio of $\dot{m}_\infty/\dot{m}_c$. The mass flux entering the boundary layer from the freestream ($\dot{m}_\infty$) is typically assumed to develop according to the $\frac{4}{5}$th law for turbulent boundary-layer growth:

$$\dot{m}_\infty = 0.329\overline{\rho}_\infty U_\infty x' Re_{x'}^{-1/5} \tag{5.7}$$

For film cooling application, it is assumed that $\dot{m}_c = \overline{\rho}_c V_c s$ where s is the slot width. Since the slot width is a constant, film cooling models are only valid starting at the trailing edge of the slot.

For film cooling, there are multiple models that employ the above assumptions, which vary based on their definition of where x' starts. These models generally assume that at the slot the effectiveness is one. Other forms of $\overline{\eta}$ that do not follow Equation 5.6 can approach a value of infinity at the slot, and are only meant to be used at some distance downstream once $\overline{\eta}$ drops below one [26]. Neither of these bode well for transpiration cooling, since there must be a finite amount of heat entering the solid inside the transpiration region. However, this generally arises due to the fact that $\dot{m}_c$ is assumed to be a constant, independent of x.

The classical film cooling effectiveness models must be modified for use inside the transpiration region. Specifically, the amount of coolant injected must be a function of the location in x. On this basis, the choice of $\dot{m}_c = \int_0^x \overline{\rho}_c V_c dx$ is made, with $x = 0$ at the leading edge of the porous plate. It is also assumed that this is the location where the turbulent boundary layer starts (*i.e.* $x' = x$). Using these assumptions, the following relationship is obtained:

$$\frac{\dot{m}_\infty}{\dot{m}_c} = 0.329\left(\frac{\overline{\rho}_\infty U_\infty x}{\int_0^x \overline{\rho}_c V_c dx}\right)^{0.8}\left(\frac{\int_0^x \overline{\rho}_c V_c dx}{\overline{\mu}_\infty}\right)^{-0.2} \tag{5.8}$$

Equation 5.8 can be substituted in to Eq. 5.6 in order to determine the cooling effectiveness due to film accumulation. The resulting cooling effectiveness has the desired form in the limit cases. As $x \to 0^+$, $\overline{\eta} \to 0$. Since no coolant has been injected yet, this is the logical value for this model. For a finite transpiration region, as $x \to \infty$, $\overline{\eta} \to 0$. For an infinitely long transpiration region, as $x \to \infty$, $\overline{\eta} \to 1$.

The derivation of Eq. 5.6 assumes that all of the coolant injected into the boundary layer is injected at the same temperature. For the present DNS data, this is consistent with the isothermal boundary condition. However, in a real situation there might be some spatial variation in the injected coolant temperature. It is possible to incorporate this effect by modifying the model.

5.2.3 Combined model

In order to consider the effects of both advection and film accumulation, the two models are combined by the relationship:

$$\overline{\eta}_{tot} = 1 - (1 - \overline{\eta}_{advect})(1 - \overline{\eta}_{film}) \tag{5.9}$$

Comparing the model for $\overline{\eta}_{tot}$ using Eq. 5.9 to the present DNS data in Fig. 5.7, it is evident that this model works reasonably well. In the transpiration region, the model closely matches the DNS data. After the transpiration zone, the effects of transpiration cooling on the heat transfer are similar to film cooling. The proposed model shifts to the film-cooling theory downstream, yielding good agreement with the DNS data there. Other cooling effectiveness models have been proposed for post-transpiration regions based on experimental data [62], however, as mentioned previously they are not consistent in the transpiration region.

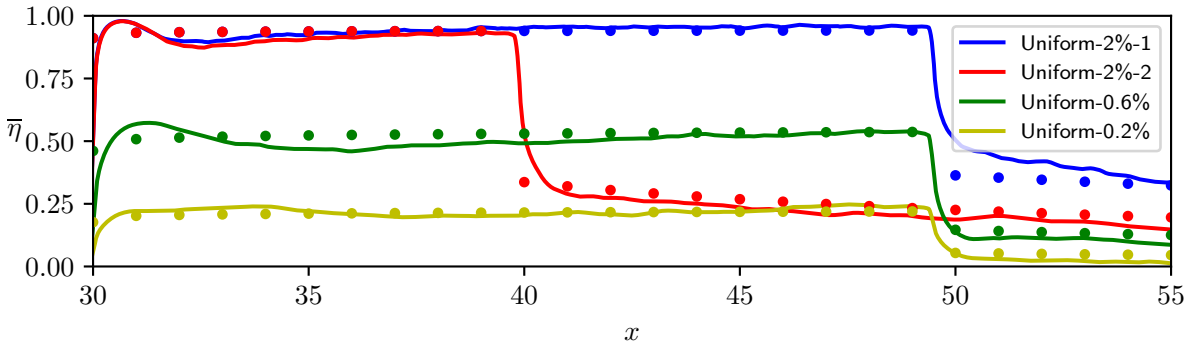

Figure 5.7: Cooling effectiveness. solid: DNS data ; dots: combined model (Eq. 5.9)

For the Uniform-2%-1 case, there is still some discrepancy in the post-transpiration region. This may be due to the fact that Eq. 5.6 does not directly account for the modification of turbulence caused by the injection of coolant. In fact, Eq. 5.5 does not account for the turbulence modification either. It is reasonable then to ask why it is expected that this model works well. The reason, as Goldstein puts it, is due to "the unwritten law that sometimes two invalid assumptions are better than one" [26]. The other invalid assumption here is that $\langle T \rangle \approx T_{w,ad}$. Additionally, it may be argued that the choice of $x' = 0$ at the leading edge of the transpiration zone is not justified based on the derivation. However,

these choices are common, and the assumptions cancel each other somewhat, yielding good results in film cooling prediction [26]. For very large modifications of the turbulence and separation of the hot flow from the wall, such as in the Uniform-2%-1 case, it would be reasonable to expect that there would be some error in using Eq. 5.9. However, the model under-predicts the DNS in the Uniform-2%-1 case downstream, and therefore provides a conservative estimate.

5.3 Log law Scaling

The injected coolant shifts the law of the wall. This shift has been studied for over half a century in the context of suction and blowing walls, and many relationships have been proposed in an attempt to generalize the problem. A summary of many of these relationships can be found in [63]. The fact that there are so many different proposed relationships speaks to the lack of a universally applicable transformation.

One way of deriving a log-law relationship is to incorporate the effect of the blowing wall on the shear stress. The assumption is that the x-momentum equation simplifies to $\overline{\rho} V_w dU/dy = d\overline{\tau}/dy$. One such relationship using the above assumptions is proposed by Stevenson [64]:

$$\frac{2}{V_w^+}(\sqrt{V_w^+ U^+ + 1} - 1) = \frac{1}{\kappa} ln(y^+) + B \tag{5.10}$$

where $V_w^+ = V_w/u_\tau$. This relationship is compared to the present data in Fig. 5.8(b), with $B = 5.1$ and $\kappa = 0.41$. For the low blowing ratio the transformation is accurate, however it is clear that this relationship fails at higher blowing ratios.

One of the possible reasons for the failure of the scaling is due to the assumptions that it is based on. For this reason, some of these assumptions will be discussed. After applying Reynolds decomposition to the Navier-Stokes momentum equations, the following equation is obtained:

$$(\overline{\rho}\,\overline{u_j} + \overline{\rho' u_j'})\frac{\partial \overline{u_i}}{\partial x_j} + \frac{\partial \overline{\rho' u_i' \overline{u_j}}}{\partial x_j} + \frac{\partial \overline{\rho' u_i' u_j'}}{\partial x_j} = -\frac{\partial \overline{p}}{\partial x_i} + \frac{\partial}{\partial x_j}(\overline{\sigma_{ij}} - \overline{\rho u_i' u_j'}) \tag{5.11}$$

In many cases, the higher order terms are neglected, resulting in:

$$(\overline{\rho}\,\overline{u_j} + \overline{\rho' u_j'})\frac{\partial \overline{u_i}}{\partial x_j} \approx -\frac{\partial \overline{p}}{\partial x_i} + \frac{\partial}{\partial x_j}(\overline{\sigma_{ij}} - \overline{\rho} \overline{u_i' u_j'}) \tag{5.12}$$

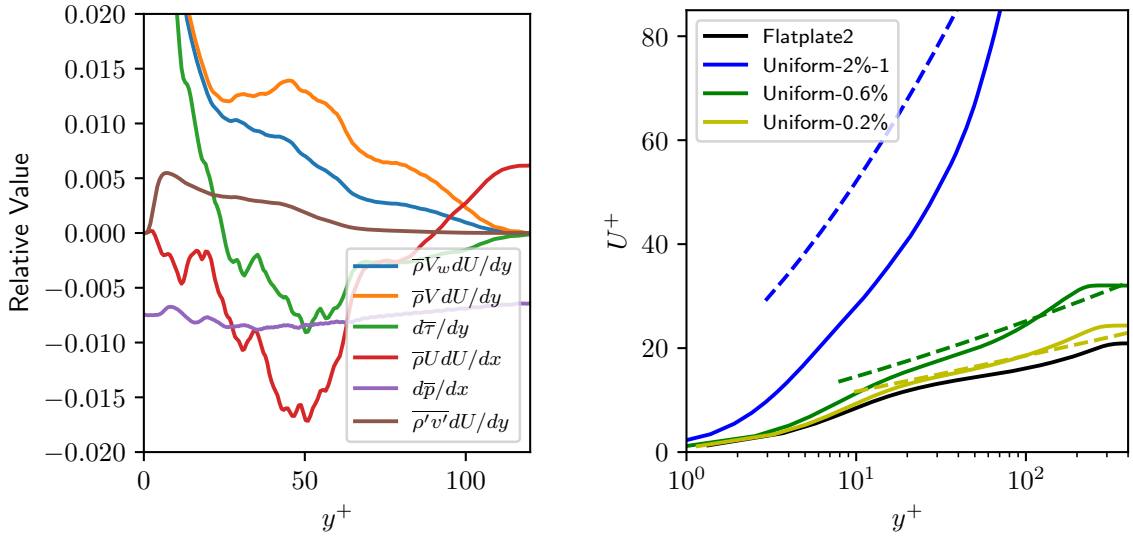

(a) Navier-Stokes x-momentum terms. Uniform-2%-2 simulation at $x = 37$.

(b) law of the wall at $x = 47$. Scaled data ——— ; Stevenson law - - - - .

Figure 5.8: Analysis of Stevenson's log-law model.

In the derivation for the blowing/suction scaling laws, the incompressible form is used (*i.e.* $\overline{\rho' u_j'} = 0$), the pressure term is neglected, the gradients in x and z are assumed negligible, and it is assumed that $\overline{u_2} = V_w$. These assumptions simplify the equation to $\overline{\rho} V_w dU/dy = d\overline{\tau}/dy$. This is then used in conjunction with the assumption of $\overline{\tau}/\overline{\rho} = (\kappa y \frac{\partial U}{\partial y})^2$ in order to derive the scaling [64].

To check these assumptions, the most significant terms in the compressible Navier-Stokes x-momentum equation have been plotted in Fig. 5.8(a). The somewhat jagged nature of some of the terms is likely due to the averaging window as discussed in Ch.4 (the gradient of shear is a sensitive value). Regardless, it is evident that the simplification of the Navier-Stokes equation to $\overline{\rho} V_w dU/dy = d\overline{\tau}/dy$ is not valid, and that the additional terms are significant. The assumption that $V = V_w$ leads to error in the log layer. This is because the hot gas is deflected upwards, creating an increase in V. Additionally, there

is a compressible term $\overline{\rho' v'}$ which is present and non-negligible. Also, due to the nature of the transpiration, there is a nonzero pressure gradient, which results in non-negligible streamwise gradients (*i.e.* $d/dx \neq 0$).

To further show that these terms are significant, plots of the average wall-normal velocity, and the average pressure for the Uniform-2%-1 case are shown in Fig. 5.9. It is clear, based on these figures, that assuming a zero gradient in pressure and in wall-normal velocity will introduce error in Eq. 5.10.

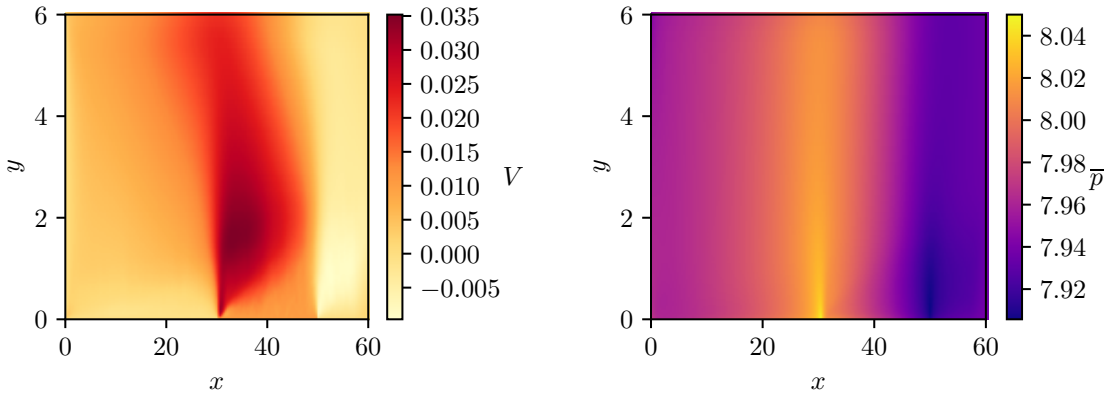

(a) average wall-normal velocity

(b) average pressure

Figure 5.9: Average plots of pressure and velocity for the Uniform-2%-1 case.

One of the integration constants in the derivation of Eq. 5.10 is chosen by Stevenson to depend on $B + 2/V_w^+$, and this choice appears arbitrary. Additionally, another constant (assumed to be unity by Stevenson) which appears inside the square root term in Eq. 5.10 would depend on the additional terms in the Navier-Stokes equations mentioned above, and therefore should generally not equal to one. However, with the addition of the extra terms, the problem becomes ill defined. Additional modelling assumptions would need to be added in order to incorporate the extra terms. Additionally, Eq. 5.10 does not collapse to the classical log-law scaling in the case that $V_w^+ = 0$. This fact is concerning, since it further limits the applicability of this model.

In conclusion, while Stevenson's law may work for modest blowing ratios, it fails to work in cases with high blowing ratios. This has been shown to be the consequence of the underlying assumptions made in the derivation of the scaling. Other scalings derived based on similar principles are also expected to have similar limitations.

5.4 Slits vs Uniform Blowing

In order to gain insight on the effect of individual pores, the slit simulations are compared with the uniform blowing simulations. This is done to assess the validity of the uniform blowing boundary condition, since simulations with pore-resolved boundary conditions are currently not feasible for practical applications. The slit width simulated here may be large (relative to the boundary layer thickness) in relation to the pore sizes which would be used in many practical transpiration cooling cases. This is simply due to computational cost. Three different slit widths were simulated in order to identify trends in the results as the pore size approaches the realistic case for transpiration cooling. The total integrated mass flow rate and porosity are kept constant for the different sized slits as discussed in Sec 3.2.

First, the effects of the slits on the flow turbulence are considered. Figure 5.10 compares the turbulent kinetic energy for all of the simulated slit cases (Fig. 5.1 shows the corresponding uniform blowing cases). The most notable difference between the uniform and slit BCs is that in the slit cases there is an area of low TKE in the near-jet region. The reason for this low TKE region is that the individual slit jets have a higher momentum than the corresponding region in the uniform BC. This means that the higher momentum coolant is able to penetrate deeper into the flow without being disturbed.

As the slit size decreases (at constant integral mass flux and porosity), the individual jets do not penetrate as deep into the domain before being broken up. This is because approximately the same (vertical) shear force per jet brakes the smaller jets faster due to their lower total momentum; or, the braking shear area increases with increasing number of slits. For the Slits-0.6%-0.5 case, there is almost no modification of the flow turbulence due to the individual slits. Additionally, it can be seen that for the lower blowing ratio ($F = 0.6\%$), the jets do not penetrate as deeply into the flow. This can also be explained by the fact that the lower blowing ratio has a lower total momentum. These factors suggest that as the pore size gets smaller and/or as the blowing ratio is reduced, the effects of the individual jets on the turbulence are also reduced.

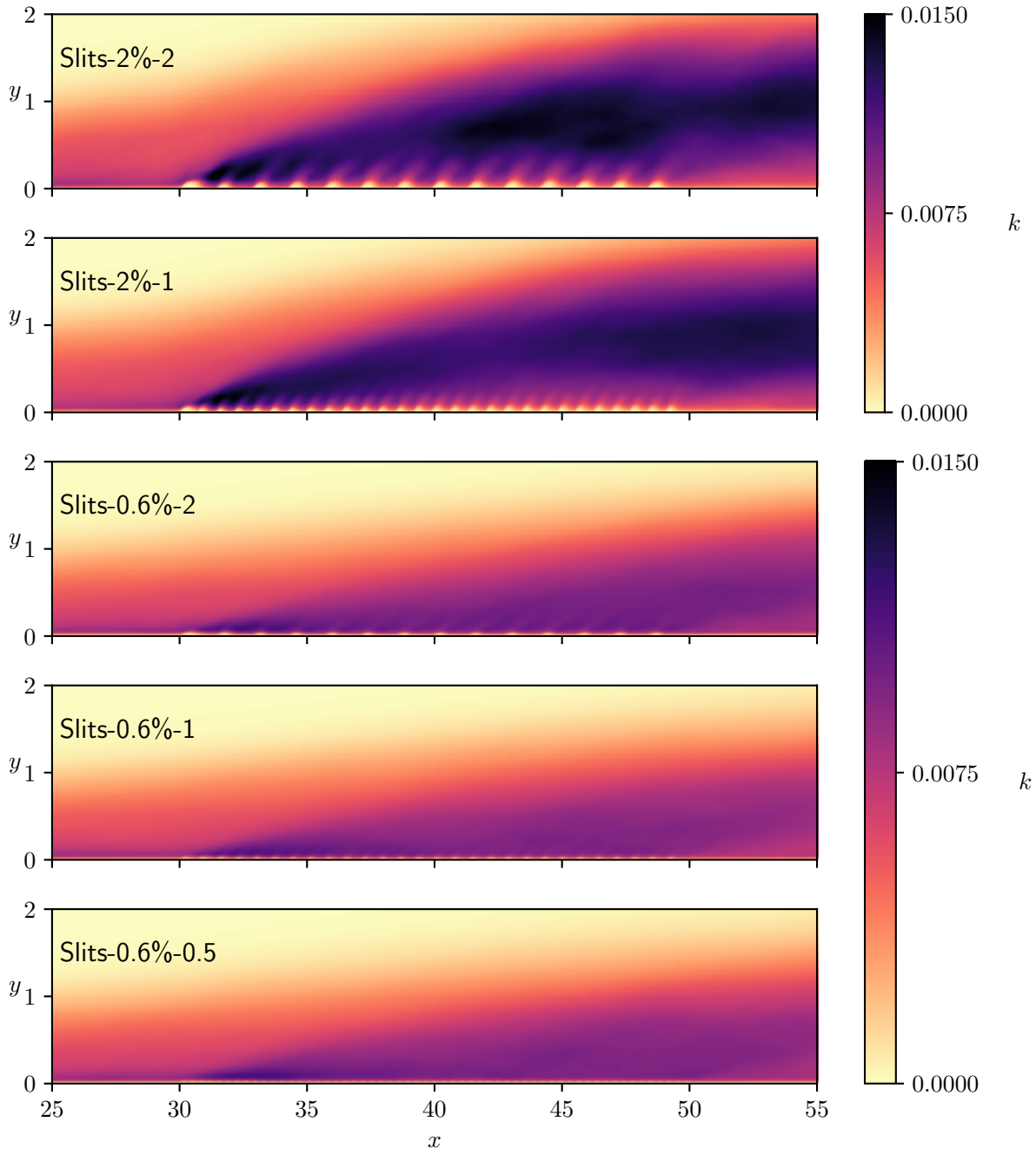

Figure 5.10: Turbulent kinetic energy comparison for different BCs.

In the rest of the flow domain, the turbulence is minimally disturbed by the difference in boundary condition. For the Slits-2%-2 case, there are some tufts of increased TKE, however there is a possibility that this is due to the averaging window as discussed in Ch.4. For the $F = 0.6\%$ cases, there is no discernible difference in the turbulence other than very close to the wall. Based on these observations, it is feasible that for small pore sizes, a uniform blowing BC can realistically predict the flow turbulence.

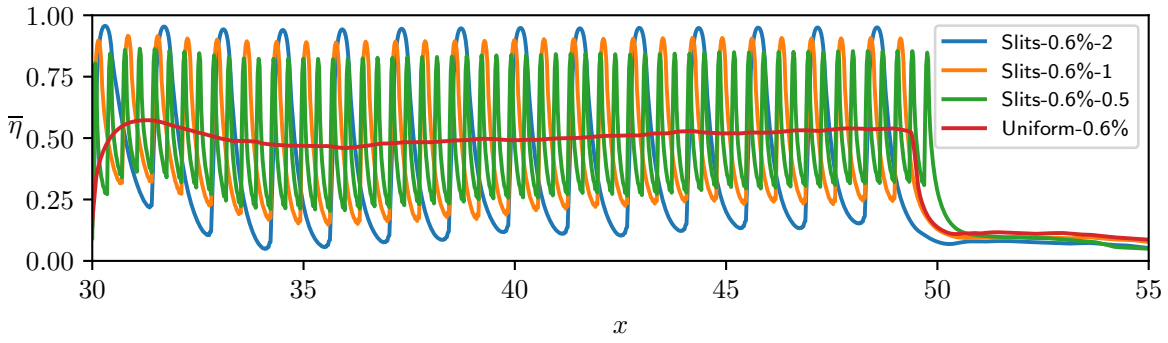

(a) $F = 0.6\%$ cases.

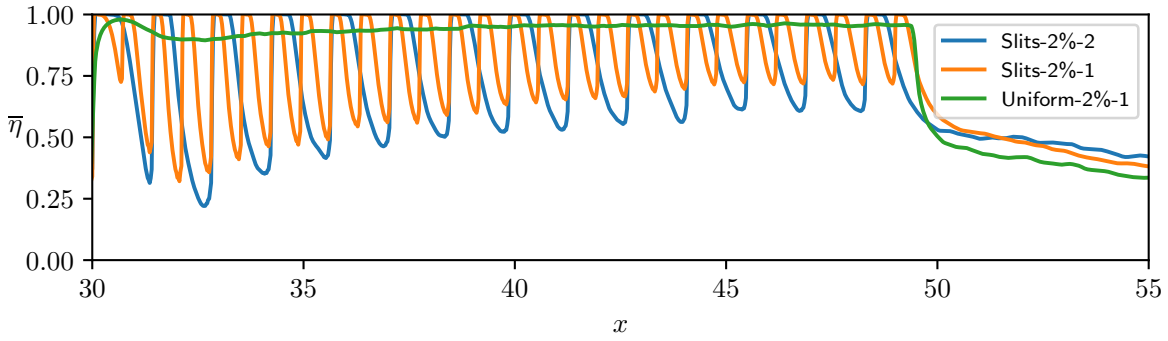

(b) $F = 2\%$ cases.

Figure 5.11: Transpiration cooling effectiveness. Comparison of boundary conditions

It is also important to consider the effect of the slits on the heat flux entering the wall. Figure 5.11(a) compares the cooling effectiveness for cases with $F = 0.6\%$. The slit cases have a periodic cooling effectiveness, which corresponds to the individual slits of injected coolant. At the region of the slit, the wall-normal velocity is high, resulting in high heat

advection and also a high cooling effectiveness. However, between the slits, the wall-normal velocity at the wall returns to zero. This means that the heat advection term disappears at the wall between the slits. As the slits get smaller in size, the amplitude of the periodic cooling effectiveness decreases. This suggests that for small jets (or pores), the cooling effectiveness plot would approach the uniform blowing case.

The average cooling effectiveness over the transpiration region (from $x_a = 30$ to $x_b = 49.6$) can also be used as a metric to compare the different boundary conditions. This is shown in Tab 5.1. It can be seen that as the jet size gets smaller, the average cooling effectiveness trends towards the uniform blowing effectiveness. Even though these slits are relatively large in relation to the boundary layer thickness, the approximation of a uniform blowing boundary condition can be justified in terms of the integrated wall heat flux for the $F = 0.6\%$ case. For the $F = 2\%$ cases, the discrepancy is much larger. This appears to be due to the fact that in the slit region, the cooling effectiveness reaches 100% for the $F = 2\%$ cases, whereas the effectiveness for the $F = 0.6\%$ cases does not (as seen in Fig. 5.11). However, the smaller slits do still trend towards the uniform case. In terms of integrated heat flux, there is still almost three times as much heat flux entering the porous plate in the Slits-2%-1 case compared to the Uniform-2%-1 case. These results highlight the difference in effectiveness between film cooling and transpiration cooling, and show that as the individual jets (or pores) get smaller, the cooling effectiveness approaches the uniform injection case.

Simulations	$\frac{1}{x_b - x_a}\int_{x_a}^{x_b} \overline{\eta} dx$
Uniform-2%-1	94%
Slits-2%-1	83%
Slits-2%-2	77%
Uniform-0.6%	50%
Slits-0.6%-0.5	48%
Slits-0.6%-1	48%
Slits-0.6%-2	44%

Table 5.1: Average cooling effectiveness over the transpiration region

It is also apparent that modification of turbulence due to the slits could affect the heat flux. For this reason, the turbulent transport of heat to the wall is considered via $\overline{v'T'}$. This is shown in Fig. 5.12. There is very little near-jet reduction in $\overline{v'T'}$ for the Slits-0.6%-2 case. For the Slits-2%-1 case, the reduction is more pronounced. Between the slits, the turbulent transport of heat near the wall returns, and the wall heat flux subsequently increases. The turbulent transport of heat appears to closely match the turbulent kinetic energy shown

in Fig. 5.10. Since temperature and velocity are highly correlated in turbulent boundary layers [37], this comparison between TKE and $\overline{v'T'}$ is reasonable.

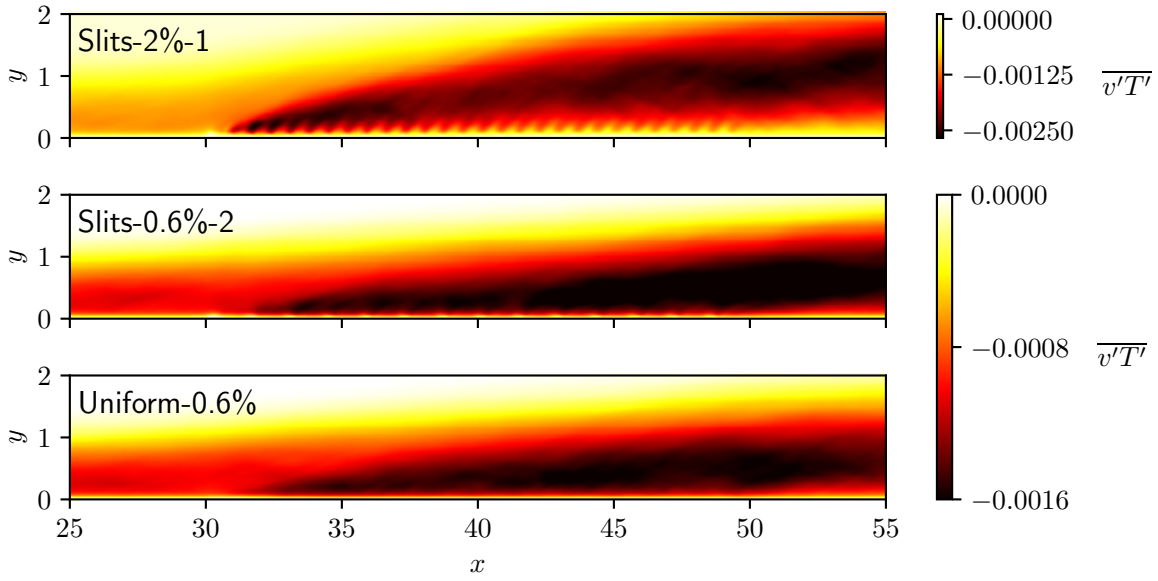

Figure 5.12: Turbulent transport of heat

5.5 Vortical structures

It is interesting to note that a peak in the cooling effectiveness near the leading edge of the transpiration region can be seen in Fig. 5.5. The peak also appears to shift closer to the leading edge as the blowing ratio is increased. This can be explained by the development of large scale vortices. The difference in velocity between the coolant and the hot gas creates vorticity. This will cause vortices to develop, transporting heat to the wall. However, there is a development time/length required for the production of these vortices. In the region before these vortices are developed, there will be a lower heat transfer rate to the wall and therefore a higher cooling effectiveness. To explain this theory, the vorticity will be investigated in this section.

The average spanwise vorticity in the Uniform-2%-1 and Uniform-0.6% cases at the leading edge of the transpiration region are plotted in Fig. 5.13. This figure clearly shows

that the near wall vorticity dominating the turbulent boundary layer upstream of the injection zone is reduced by the coolant. This is because the injected coolant gas reduces the near-wall velocity gradient and consequently reduces the local wall shear stress. A shear/vorticity layer created by the velocity difference between the coolant and the hot gas can be seen in the Uniform-2%-1 case. This results in a region of low vorticity between $x = 30$ to $x = 31$ very close to the wall for the Uniform-2%-1 case. This coincides with the peak in cooling effectiveness seen in Fig. 5.5. A bit farther downstream, there is an increase in the average spanwise vorticity near the wall, but the level is still much lower than that of the incoming undisturbed boundary layer. For the Uniform-0.6% case, it is apparent that the wall vorticity decreases, but there is no trough in vorticity near the leading edge of the plate. To explain why there is still a peak in cooling effectiveness here, the vortical structures must be identified from the instantaneous snapshots of the flow.

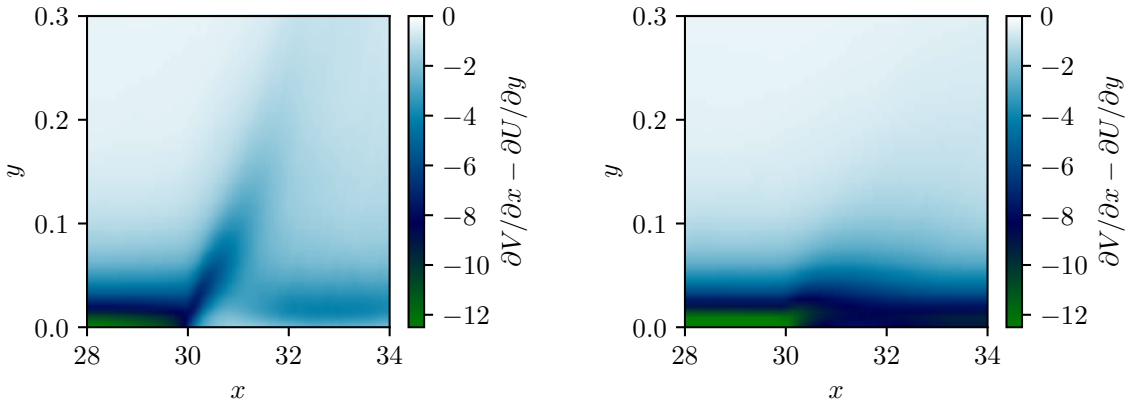

(a) Uniform-2%-1 case

(b) Uniform-0.6% case

Figure 5.13: Average spanwise vorticity

It is important to consider the instantaneous large scale vortical structures in the flow. This can be done by calculating the λ_2-criterion, which is commonly used to identify vortex cores [65]. The λ_2-criterion is derived by taking the gradient of the Navier-Stokes equations, and then decomposing the acceleration gradient into its symmetric and antisymmetric components. Considering a vortex core as the pressure minimum due to vortical motion, the relevant terms in the symmetric component are [66]:

$$S_{ik}S_{kj} + \Omega_{ik}\Omega_{kj} = -\frac{1}{\rho}p_{ij} \tag{5.13}$$

Here, $S_{ij} = \frac{1}{2}(\frac{\partial u_i}{\partial x_j} + \frac{\partial u_j}{\partial x_i})$ is the rate-of-strain tensor, and $\Omega_{ij} = \frac{1}{2}(\frac{\partial u_i}{\partial x_j} - \frac{\partial u_j}{\partial x_i})$ is the vorticity tensor. A vortex core is identified if there are at least two negative eigenvalues of the 3x3 matrix $S_{ik}S_{kj} + \Omega_{ik}\Omega_{kj}$. Therefore, by defining $\lambda_3 \leq \lambda_2 \leq \lambda_1$, the criteria for identifying a vortex core becomes that $\lambda_2 < 0$. This is also equivalent to positive values of the Q-criterion, which is a similar vortex core identification method [66].

In this section, a threshold value of $-\lambda_2 > 2$ is used to identify strong vortices. A plot of the $-\lambda_2 = 2$ iso-surface for snapshots of the flow at different blowing ratios can be seen in Fig 5.14. Note that only 1/2 of the domain in z has been plotted, as well as only 3/10 of the domain in x, and the iso-surface is coloured by y position. It is evident that the amount of vortical structures increases with blowing rate. For the Uniform-0.2% case there is no significant increase in the vortical structures based on visual inspection. For the Uniform-0.6% case it appears that both near the wall, and farther into the boundary layer, the structures are increased. The Uniform-2%-1 case has a much more drastic increase in vortical structures compared to the other cases.

In order to show the λ_2 results in a more quantitative way, the spatial probability of $-\lambda_2 > 2$ for a given position in x is calculated via:

$$P(-\lambda_2 > 2|x = X) = \frac{1}{36}\int_0^6 \int_0^6 H(-\lambda_2(X, y, z) - 2)dydz \tag{5.14}$$

Here, H is the Heaviside function. The probabilities are averaged over 30 snapshots of the flow, spaced in time by $\triangle t = 1$. The result is plotted in Fig 5.15. It can be seen that there is a large production of vortices in the transpiration region. At the leading edge of this region, there is some delay before these vortices are produced. This delay in the production of vortices appears to coincide with the peak in cooling effectiveness near the leading edge of the plate as can be seen in Fig. 5.7.

The rapid growth of vortical structures near the front of the plate also appears to coincide with the local minimum in the cooling effectiveness seen in Fig. 5.7. While the amount of vortices after this point still grow, they grow at a slower rate. Some of this additional growth may be explained by the increasing thickness of the boundary layer due to the addition of coolant. Since the film cooling effectiveness grows with x, it counteracts the effects of the turbulent transport of heat, creating this local minimum in the cooling effectiveness.

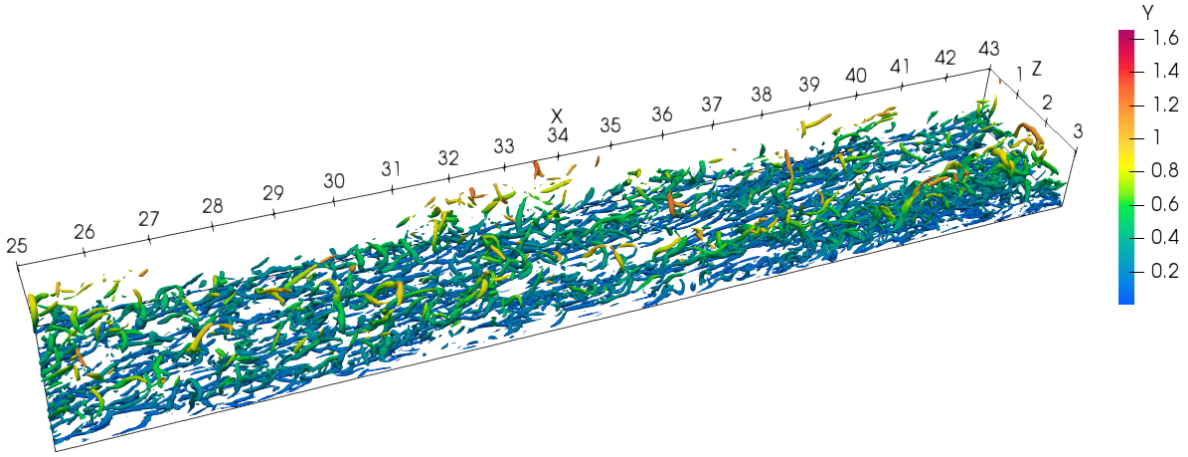

(a) Uniform-0.2% case

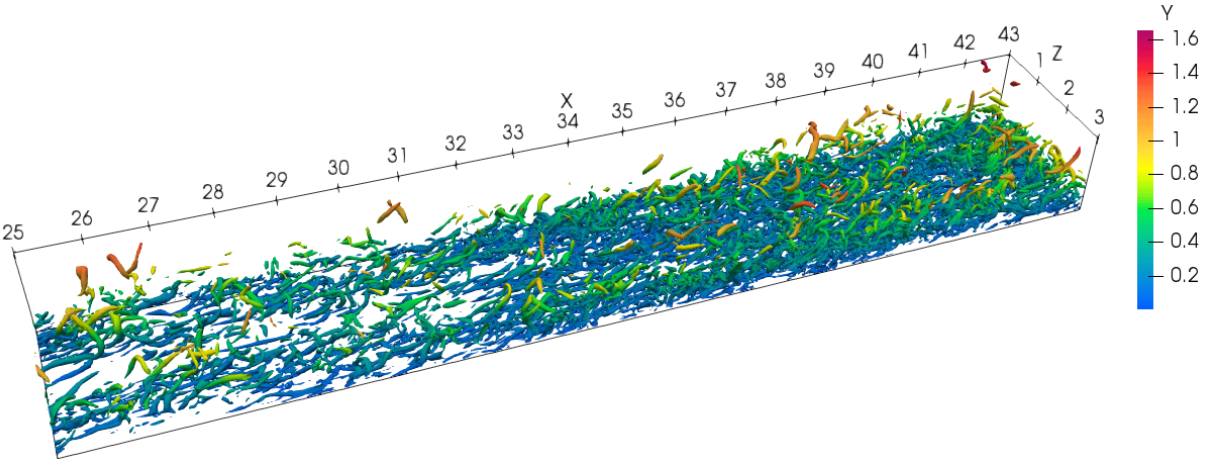

(b) Uniform-0.6% case.

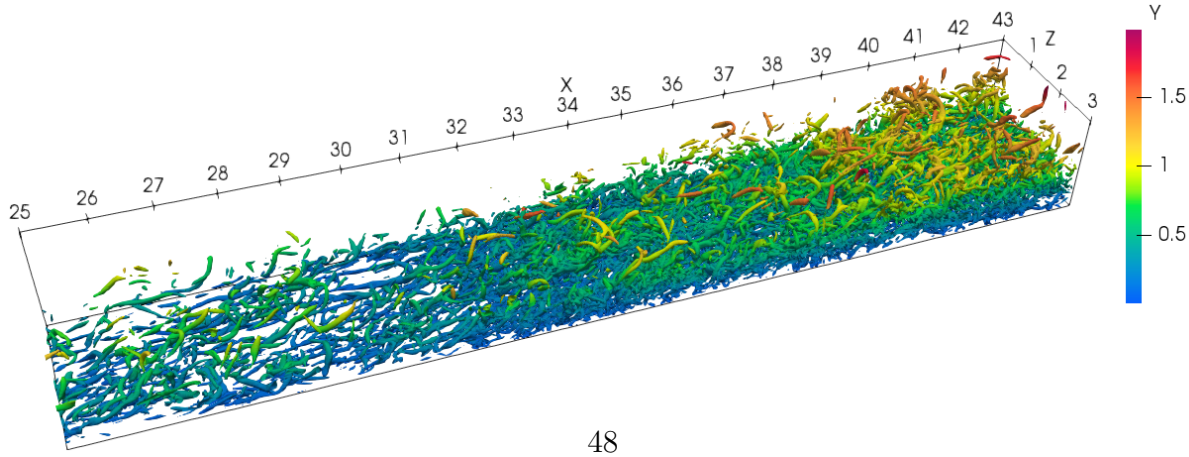

(c) Uniform-2%-1 case

Figure 5.14: Iso-surface of $-\lambda_2 = 2$

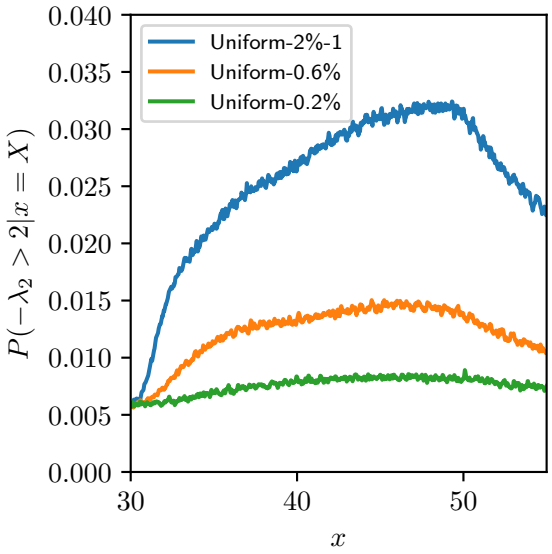

Figure 5.15: Probability of $-\lambda_2 > 2$ vs x

To supplement the λ_2 analysis, Fig. 5.12 shows that the production of vortices also coincides with the region where the turbulent transport of heat to the wall increases significantly in the flow. It is apparent based on this analysis that the modification to the turbulent transport of heat due to vortical structures acts to decrease the cooling effectiveness in the flow.

In a real situation, there may be a lower mass flux near the leading edge of the plate due to pressure [67], and so the peak in cooling effectiveness may not be observed. However, this would greatly depend on the permeability of the porous material; the higher the flow restriction the the porous material is, the more uniform the velocity distribution would be. Experimentally, there would also be other effects such as heat transfer through the side walls, and biases in the porous material properties near the plate edges due to sintering, which could cause the opposite trend in cooling effectiveness near the leading edge to be observed.

Chapter 6

Conclusions

Direct Numerical Simulations of transpiration cooling in a spatially-developing turbulent flat-plate boundary layer have been performed. These simulations serve to gain insight into the physics of transpiration cooling, and to analyze and propose modelling strategies for heat flux and velocity boundary conditions for practical CFD models.

At low blowing ratios (*i.e.* $F = 0.2\%$), there is a small increase in the TKE in comparison to the reference isothermal flat-plate case due to the shear interaction between the coolant and the hot gas. At higher blowing ratios (*i.e.* $F = 2\%$) the hot gas flow separates from the wall, and the peak in TKE is caused by the interaction between high-momentum hot gas and low-momentum coolant gas (rather than the shear at the wall).

There are effectively two mechanisms which contribute to the reduction of wall heat transfer in the transpiration zone. The first is the reduction in average temperature of the boundary layer due to the injected coolant. An equation for predicting this effect has been proposed, and is consistent in the limit cases. The second heat reduction mechanism is heat advection away from the wall. In the transpiration zone, this appears to be the dominating heat-transfer reduction mechanism. The DNS data reasonably match the combined model of cooling effectiveness, despite neglecting the change in turbulent transport of heat.

Many log law scalings have been proposed over the years for blowing walls. One classical scaling proposed by Stevenson [64] has been compared to the present DNS data, and shown to only work for low blowing ratios. By analyzing the terms in the x-momentum Navier-Stokes equation, it is shown that the underlying assumptions of Stevenson's scaling (and other scalings that use similar derivations) do not hold for high blowing ratios.

Comparing the cases simulated with uniform injection to the cases with blowing by discrete slits (at the same total mass flow rate), some differences are apparent. The TKE

is reduced near the slits due to the relatively high wall-normal momentum of the coolant. Additionally, the increased heat advection away from the wall at the slits increases the cooling effectiveness in that region, but the effectiveness between the slits is decreased due to the absence of heat advection. These effects are mitigated by decreasing the slit width (at constant integral coolant mass flux and fixed porosity). It is hypothesized that for small pore sizes, the use of uniform blowing BCs is realistic.

The turbulent transport of heat due to the production of unsteady vortices is investigated. There are vortical structures created due to the interaction between hot gas and coolant. It is apparent that the turbulent transport of heat is modified due to the production of these vortices. By considering the cooling effectiveness at the leading edge of the plate, it can be seen that the increase in turbulent transport of heat due to these vortices results in a decrease in cooling effectiveness.

Chapter 7

Recommendations

Throughout this work, additional questions arose that could be used as topics for future research. Therefore, the following topics are recommended for future researchers:

- Running additional DNS simulations investigating the supersonic/hypersonic regime. This would be of interest due to the application of transpiration cooling to re-entry vehicles. The code could relatively easily accommodate this, since WENO schemes are already implemented.
- Analysis on turbulence modelling for RANS simulations of transpiration cooling. This could be done by running RANS simulations and comparing to the DNS data. Additionally, the assumptions of the turbulence models could be analyzed by plotting relevant terms using the DNS data.
- Simulations with different fluids for the coolant and hot gas. Using water or fuel for the coolant is more practical than air in re-entry applications. Therefore, DNS simulations investigating these species would be useful. The code used in this work does not include multi-species capability, so this would either need to be added to the code, or another code could be used.
- Coupling with a porous media solver. The DNS solver could be coupled with a porous media solver in order to give more realistic injection BCs.
- Additional analysis on the inner scaling for the law of the wall. While it was shown that proposed models do not work for the high blowing rates, no sufficient model was identified. Future work could include additional analysis on this. Also, analysis on

the compressible transformation by Trettel and Larsson [55] could be done to identify the reason for error in the hypersonic regime, and to propose modifications.

- Development of a two-phase coolant porous media solver, and coupling with a multi-species RANS solver. Currently, there is no software available for this. This may be due to the fact that the most common two-phase porous media solver (the TPMM) still has un-resolved issues associated with it. In some applications, it may be the case that all of the liquid coolant flashes to vapor upstream of the porous media due to heat conduction/diffusion. In this case, development toward coupling of multi-species/multi-phase RANS solvers to a single phase porous media solver would also be useful. Development of these capabilities is crucial for aerospace applications.

References

[1] N. Christopher, J. Peter, M. Kloker, and J.-P. Hickey. Investigation of transpiration cooling in turbulent flow by DNS. In *Proceedings of the 2019 SFB TRR40 Summer Program*, 2019 (in press).

[2] N. Christopher, J. Peter, M. Kloker, and J.-P. Hickey. DNS of Turbulent Flat-Plate Flow with Transpiration Cooling. *Manuscript submitted for publication*, 2019.

[3] Ultramet. Liquid Rocket Engines. https://ultramet.com/propulsion-system-components/liquid-rocket-engines/, 2018. Accessed: 2019-03-13.

[4] Je-Chin Han and Akhilesh Rallabandi. Turbine blade film cooling using psp technique. *Frontiers in Heat and Mass Transfer (FHMT)*, 1(1), 2010.

[5] David G Bogard and Karen A Thole. Gas turbine film cooling. *Journal of propulsion and power*, 22(2):249–270, 2006.

[6] Ernst Rudolf Georg Eckert and John NB Livingood. Comparison of effectiveness of convection-, transpiration-, and film-cooling methods with air as coolant. *NACA, Report 1182*, 1954.

[7] Zheng Min, Gan Huang, Sarwesh Narayan Parbat, Li Yang, and Minking K. Chyu. Experimental investigation on additively manufactured transpiration and film cooling structures. *Journal of Turbomachinery*, 141(3):1–10, 2019.

[8] Rob Stein and Guy Gugliotta. Ceramic shuttle tiles had history of glitches. *Washington Post*, page A01, Feb 2003.

[9] D'Agostino, Ryan. Elon Musk: Why I'm Building the Starship out of Stainless Steel. https://www.popularmechanics.com/space/rockets/a25953663/elon-musk-spacex-bfr-stainless-steel/, 2019. Accessed: 2019-11-05.

[10] Arnold van Foreest, Martin Sippel, Josef Klevanski, Ali Gülhan, and Burkard Esser. Transpiration cooling to handle the aerothermodynamic challenges of the spaceliner concept. In *2nd European Conference for Aerospace Sciences (EUCASS)*, 2007.

[11] George P Sutton and Oscar Biblarz. *Rocket propulsion elements*. John Wiley & Sons, 2016.

[12] Charles J Obrien. Transpiration and regenerative cooling of rocket engine. *NASA tech briefs*, 13(8):75, 1989.

[13] Armin Herbertz, Markus Ortelt, Ilja Müller, and Hermann Hald. c*-Efficiency evaluation of transpiration cooled ceramic combustion chambers. *CEAS Space Journal*, 6(2):99–105, 2014.

[14] Valentina König, Sebastian Muller, and M. Rom. Numerical investigation of transpiration cooling in supersonic nozzles. In *Sonderforschungsbereich/Transregio 40 – Annual Report 2018*, 2018.

[15] Yukinori Kametani, Koji Fukagata, Ramis Örlü, and Philipp Schlatter. Effect of uniform blowing/suction in a turbulent boundary layer at moderate Reynolds number. *International Journal of Heat and Fluid Flow*, 55:132–142, 2015.

[16] Haecheon Choi, Parviz Moin, and John Kim. Active turbulence control for drag reduction in wall-bounded flows. *Journal of Fluid Mechanics*, 262:75–110, 1994.

[17] Viola Wartemann, Giannino Ponchio Camillo, Philipp Reiter, Jens Neumann, and Alexander Wagner. Influence of transpiration cooling on second-mode instabilities investigated on hypersonic, conical flows. *CEAS Space Journal*, 11(3):341–350, 2019.

[18] David C Wilcox et al. *Turbulence modeling for CFD*, volume 3. DCW industries Inc, 2006.

[19] W. Dahmen, S. Müller, M. Rom, S. Schweikert, M. Selzer, and J. Von Wolfersdorf. Numerical boundary layer investigations of transpiration-cooled turbulent channel flow. *International Journal of Heat and Mass Transfer*, 86:90–100, 2015.

[20] V. Avsarkisov, M. Oberlack, and S. Hoyas. New scaling laws for turbulent Poiseuille flow with wall transpiration. *Journal of Fluid Mechanics*, 746:99–122, 2014.

[21] S. Kraheberger, S. Hoyas, and M. Oberlack. DNS of a turbulent Couette flow at constant wall transpiration up to Re_τ=1000. *Journal of Fluid Mechanics*, pages 421–443, 2017.

[22] Adriano Cerminara, Ralf Deiterding, and Neil Sandham. Direct numerical simulation of hypersonic flow through regular and irregular porous surfaces. In *Proceedings of the Seventh European Conference on Computational Fluid Dynamics, ECCOMAS ECFD 2018*, 06 2018.

[23] Adriano Cerminara, Ralf Deiterding, and Neil Sandham. Parallel multiscale simulation of hypersonic flow with porous wall injection. In P. Ivanyi and B.H.V. Topping, editors, *Proceedings of the Sixth International Conference on Parallel, Distributed, GPU and Cloud Computing for Engineering*, volume 112, United Kingdom, 6 2019. Civil-Comp Press.

[24] Meng Zhang, Chen-nan Sun, Xiang Zhang, Phoi Chin Goh, Jun Wei, Hua Li, and David Hardacre. Competing influence of porosity and microstructure on the fatigue property of laser powder bed fusion Stainless Steel 316L. *Solid Freeform Fabrication Symposium*, pages 365–376, 2017.

[25] Xi-Shu Wang. Fatigue Cracking Behaviors and Influence Factors of Cast Magnesium Alloys. In *Special Issues on Magnesium Alloys*, volume 1, page 90. 2011.

[26] Richard J Goldstein. Film Cooling. volume 7 of *Advances in Heat Transfer*, pages 321–379. Elsevier, 1971.

[27] Tatsuaki Furumoto, Ayato Koizumi, Mohd Rizal Alkahari, Rui Anayama, Akira Hosokawa, Ryutaro Tanaka, and Takashi Ueda. Permeability and strength of a porous metal structure fabricated by additive manufacturing. *Journal of Materials Processing Technology*, 219:10–16, 2015.

[28] Armin Herbertz, Markus Ortelt, Ilja Müller, and Hermann Hald. Potential applications of the ceramic thrust chamber technology for future transpiration cooled rocket engines. *Trans Jpn Soc Aeronaut SpaceSci Aerospace Technol Jpn*, 10(ists28):Ta_7–Ta_15, 2012.

[29] Web of Science. http://webofknowledge.com/WOS, 2019. Accessed: 2019-11-05.

[30] Mihaela Vlasea, Ahmad Basalah, Amir Azhari, Rita Kandel, and Ehsan Toyserkani. Additive Manufacturing for Bone Load Bearing Applications. *3D Bioprinting and Nanotechnology in Tissue Engineering and Regenerative Medicine*, pages 231–263, 2015.

[31] S. Gulli and L. Maddalena. Arc-jet testing of a variable-transpiration-cooled and uncoated carbon-carbon nose cone. *Journal of Spacecraft and Rockets*, 56(3):780–788, 2019.

[32] J. H. Wang and H. N. Wang. A Discussion of Transpiration Cooling Problems through an Analytical Solution of Local Thermal Nonequilibrium Model. *Journal of Heat Transfer*, 128(10):1093, 2006.

[33] HS Mickley. Heat, mass, and momentum transfer for flow over a flat plate with blowing or suction. *NACA, TN 3208*, 1954.

[34] William Morrow Kays and M E Crawford. *Convective heat and mass transfer*. McGraw-Hill Inc., 3rd edition, 1993.

[35] WD Rannie, Louis G Dunn, and Clark B Millikan. A simplified theory of porous wall cooling. Technical report, Pasadena, CA: Jet Propulsion Laboratory, National Aeronautics and Space Administration, 1947.

[36] Joseph Friedman. A theoretical and experimental investigation of rocket-motor sweat cooling. *Jour. Am. Rocket Soc*, (79):147–154, 1949.

[37] Ernst Rudolf Georg Eckert. *Introduction to the Transfer of Heat and Mass*. McGraw-Hill, 1950.

[38] Tobias Langener, Jens Von Wolfersdorf, and Johan Steelant. Experimental investigations on transpiration cooling for scramjet applications using different coolants. *AIAA journal*, 49(7):1409–1419, 2011.

[39] John Parry, Robin B Bornoff, Peter Stehouwer, Lonneke T Driessen, and Erwin Stinstra. Simulation-based design optimization methodologies applied to cfd. *IEEE transactions on components and packaging technologies*, 27(2):391–397, 2004.

[40] Zhengwen Zeng and Reid Grigg. A criterion for non-darcy flow in porous media. *Transport in porous media*, 63(1):57–69, 2006.

[41] J X Shi and J H Wang. A Numerical Investigation of Transpiration Cooling with Liquid Coolant Phase Change. *Transport in Porous Media*, 87(3):703–716, 2011.

[42] Omar Rafae Alomar, Miguel A A Mendes, Dimosthenis Trimis, and Subhashis Ray. Numerical simulation of complete liquid-vapour phase change process inside porous media using smoothing of diffusion coefficient. *International Journal of Thermal Sciences*, 86:408–420, 2014.

[43] Wenjie Dong and Jianhua Wang. A New Model and its Application to Investigate Transpiration Cooling with Liquid Coolant Phase Change. *Transport in Porous Media*, 122(3):575–593, 2018.

[44] Florian Menter. Zonal two equation kw turbulence models for aerodynamic flows. In *23rd fluid dynamics, plasmadynamics, and lasers conference*, page 2906, 1993.

[45] Rui Ding, Jianhua Wang, Fei He, Guangqi Dong, and Longsheng Tang. Numerical investigation on the performances of porous matrix with transpiration and film cooling. *Applied Thermal Engineering*, 146(September 2018):422–431, 2019.

[46] Stephen B Pope. *Turbulent Flows*. Cambridge University Press, 2000.

[47] N. Christopher, J.-P. Hickey, S. De Graaf, Josette Bellan, W. K. Bushe, C. Devaud, and V. Hannemann. Probability Density Function Characterization for Conditional Source-term Estimation in High-Pressure Combustion. In *Proceedings of the 2017 SFB TRR40 Summer Program*, 2017.

[48] Chao Zhang, Lian Duan, and Meelan M Choudhari. Direct Numerical Simulation Database for Supersonic and Hypersonic Turbulent Boundary Layers. *AIAA Journal*, 56(11):1–15, 2018.

[49] Yasushi Sumitani and Nobuhide Kasagi. Direct numerical simulation of turbulent transport with uniform wall injection and suction. *AIAA journal*, 33(7):1220–1228, 1995.

[50] Yukinori Kametani and Koji Fukagata. Direct numerical simulation of spatially developing turbulent boundary layers with uniform blowing or suction. *Journal of Fluid Mechanics*, 681:154–172, 2011.

[51] I. Bermejo-Moreno, J. Bodart, J. Larsson, B. M. Barney, J. W. Nichols, and S. Jones. Solving the compressible navier-stokes equations on up to 1.97 million cores and 4.1 trillion grid points. In *SC '13: Proceedings of the International Conference on High Performance Computing, Networking, Storage and Analysis*, pages 1–10, Nov 2013.

[52] Ken Mattsson, Magnus Svärd, and Jan Nordström. Stable and accurate artificial dissipation. *J. Sci. Comput.*, 21:57–79, 08 2004.

[53] Javier Jiménez, Sergio Hoyas, Mark P. Simens, and Yoshinori Mizuno. Turbulent boundary layers and channels at moderate Reynolds numbers. *Journal of Fluid Mechanics*, 657:335–360, 2010.

[54] E R van Driest. Turbulent Boundary Layer in Compressible Fluids. *Journal of Aeronautical Sciences*, 18(3):145–160, 1951.

[55] Andrew Trettel and Johan Larsson. Mean velocity scaling for compressible wall turbulence with heat transfer. *Physics of Fluids*, 28(2), 2016.

[56] Davide Modesti and Sergio Pirozzoli. Reynolds and Mach number effects in compressible turbulent channel flow. *International Journal of Heat and Fluid Flow*, 59:33–49, 2016.

[57] Mark V Morkovin. Effects of compressibility on turbulent flows. *Mécanique de la Turbulence*, 367:380, 1962.

[58] Christoph Wenzel, Björn Selent, Markus Kloker, and Ulrich Rist. Dns of compressible turbulent boundary layers and assessment of data/scaling-law quality. *Journal of Fluid Mechanics*, 842:428–468, 2018.

[59] M. F. Shahab, G. Lehnasch, T. B. Gatski, and P. Comte. Statistical characteristics of an isothermal, supersonic developing boundary layer flow from DNS data. *Flow, Turbulence and Combustion*, 86(3-4):369–397, 2011.

[60] Duosi Fan, Jinglei Xu, Matthew Yao, and Jean-Pierre Hickey. On the detection of internal interfacial layers in turbulent flows. *Journal of Fluid Mechanics*, 872:198–217, 04 2019.

[61] Matthew Yao, Zeping Sun, Carlo Scalo, and Jean-Pierre Hickey. Vortical and thermal interfacial layers in wall-bounded turbulent flows under transcritical conditions. *Phys. Rev. Fluids, Accepted: 15 July 2019*, 2019.

[62] R. J. Goldstein, G. Shavit, and T. S. Chen. Film-Cooling Effectiveness With Injection Through a Porous Section. *Journal of Heat Transfer*, 87(3):353, 1965.

[63] Marco Ferro. *Experimental study on turbulent boundary-layer flows with wall transpiration.* PhD thesis, KTH Royal Institute of Technology, 2017.

[64] T.N. Stevenson. A law of the wall for turbulent boundary layers with suction or injection. *Cranfield College of Aero.*, (166), 1963.

[65] Jie Yao and Fazle Hussain. Toward vortex identification based on local pressure-minimum criterion in compressible and variable density flows. *Journal of Fluid Mechanics*, 850:5–17, 2018.

[66] Jinhee Jeong and Fazle Hussain. On the identification of a vortex. *Journal of fluid mechanics*, 285:69–94, 1995.

[67] Michael A. Keller and Markus J. Kloker. Effusion Cooling and Flow Tripping in Laminar Supersonic Boundary-Layer Flow. *AIAA Journal*, 53(4):902–919, 2014.

Appendix A

Sampling uncertainty

It is always important to verify that results are statistically significant. Statistical uncertainty due to sampling can cause the predicted mean value to deviate from the actual mean value. The equation to determine the uncertainty in the estimate of a quantity $\overline{\phi}$ is:

$$SE_\phi = \sigma_\phi / \sqrt{N} \tag{A.1}$$

Where SE_ϕ is the uncertainty (*i.e.* standard error) on the mean, σ_ϕ is the standard deviation, and N is the number of samples.

Since the heat flux and cooling efficiency are of importance, and both are mean quantities, these are used to determine the sampling uncertainty. In the DNS, the ratio of heat flux between the reference flatplate case and the cases with transpiration cooling can be used to compute the cooling effectiveness:

$$\eta = 1 - \left. \frac{q_{transpiration}}{q_{flatplate}} \right|_w \tag{A.2}$$

In order to determine the variance in cooling efficiency, the variance in each independent variable which influences the cooling efficiency must be combined using the following relationship:

$$\sigma_\eta = \sqrt{\left(\frac{\partial \eta}{\partial q_{transpiration}}\right)^2 \sigma^2_{q_{transpiration}} + \left(\frac{\partial \eta}{\partial q_{flatplate}}\right)^2 \sigma^2_{q_{flatplate}}} \tag{A.3}$$

The heat flux is calculated by $q_w = \lambda dT/dy|_w$, where λ is the thermal conductivity. While the calculation of the temperature gradient for post processing is done with a second-order scheme, for simplicity it is assumed here that

$$q_w = \lambda_w \frac{T_{w+1} - T_w}{y_{w+1} - y_w} \tag{A.4}$$

Since T_w (and therefore also λ_w) is fixed, the only quantity with variance is T_{w+1}. Therefore, the heat flux variance can be estimated using:

$$\sigma_{q_w} = \sqrt{(\frac{\partial q_w}{\partial T_{w+1}})^2 \sigma^2_{T_{w+1}}} \tag{A.5}$$

By applying this analysis to the data for the Uniform-2%-1 case, the maximum σ_η is approximately 0.6. The data has been sampled sequentially in time at approximately 13,000 snapshots (which is approximately one large eddy turnover time), and at every z location (since the mean flow properties are not expected to change in that direction). This means than the number of samples $N \approx 3,000,000$. Therefore, the uncertainty in the averaged value of η due to sample size is at most $SE_\eta \approx \pm 0.0003$. This uncertainty is at negligible levels.